

**A&A manuscript no.**  
(will be inserted by hand later)

**Your thesaurus codes are:**

# On radial gas flows, the Galactic Bar and chemical evolution in the Galactic Disc

L. Portinari and C. Chiosi

Department of Astronomy, University of Padova, Vicolo dell'Osservatorio 5, 35122 Padova, Italy (portinari, chiosi@pd.astro.it)

Received 23 August 1999/ Accepted 14 January 2000

**Abstract.** We develop a numerical chemical model allowing for radial flows of gas, with the aim to analyse the possible role of gas flows in the chemical evolution of the Galactic Disc. The dynamical effects of the Galactic Bar on the radial gas profile of the Disc are especially addressed.

**Key words:** Galaxy: chemical evolution – Galaxy: abundance gradients – Galaxy: gas distribution – Galaxy: Bar

## 1. Introduction

The observed chemical and spectro-photometric properties of galaxies are one of the main sources of information for our understanding of galaxy formation and evolution. The corresponding theoretical modelling involves star formation (SF) as a basic ingredient. Unfortunately, this process is rather poorly known on the large scales relevant to galaxy evolution. Portinari & Chiosi (1999, hereinafter PC99) analysed the effects of adopting different SF laws in a chemical model for the Galactic Disc, a system which we can study in great detail. In this paper we address another phenomenon which can bear interesting effects on the chemical evolution of galaxies: radial gas flows. A few papers in literature (Section 2) demonstrate that radial gas flows influence chemical models for the Disc, especially in their predictions on the metallicity gradient. It is therefore interesting to discuss the radial profile of the Disc with models including also radial flows, in addition to various options for the SF law. In particular, radial flows can help to overcome some difficulties that “static” models find in reproducing, at the same time, the metallicity gradient and the radial gas profile of the Disc (PC99).

We develop a chemical model with radial gas flows as a multi-dimensional extension of the model of Portinari et al. (1998, hereinafter PCB98). The model is described in Section 3 and in the appendices. In Section 4 we discuss the general qualitative effects of superposing radial flows upon a chemical model. In Section 5 we present models for

the Galactic Disc with radial gas flows and different SF laws, showing that radial flows provide an alternative or additional dynamical effect to the “inside-out” formation scenario to explain the metallicity gradient. Section 6 is dedicated to qualitative simulations of the dynamical effects of the Galactic Bar upon the gas distribution, with the aim to reproduce the molecular ring around 4 kpc, which static models cannot account for (PC99). Section 7 contains a final summary and conclusions.

## 2. Radial flows: previous literature

The possibility that radial flows play a role in establishing the radial metallicity gradients in galactic discs was first suggested by Tinsley & Larson (1978). Following Lacey & Fall (1985), we mention that radial gas flows in a disc can be driven by three main mechanisms:

1. the infalling gas has a lower angular momentum than the circular motions in the disc, and mixing with the gas in the disc induces a net radial inflow with a velocity up to a few  $\text{km sec}^{-1}$ ;
2. viscosity in the gas layer induces radial inflows in the inner parts of the disc and outflows in the outer parts, with velocities of  $\sim 0.1 \text{ km sec}^{-1}$ ;
3. gravitational interactions between gas and spiral density waves lead to large-scale shocks, dissipation and therefore radial inflows of gas (or outflows in the outer parts) with typical velocities of  $\sim 0.3 \text{ km sec}^{-1}$  (e.g. Bertin & Lin 1996 and references therein); much larger velocities can be achieved in the inner few kpc in the presence of a barred potential.

In summary, radial flows are plausible with velocities of  $\sim 0.1\text{--}1 \text{ km sec}^{-1}$ , and they are expected to be inflows over most of the disc. Observational upper limits permit radial inflows in the Galactic Disc with velocities up to  $5 \text{ km sec}^{-1}$  at the present time. For further details, see Lacey & Fall (1985) and references therein.

The first of the above mentioned mechanisms was modelled in detail by Mayor & Vigroux (1980), and later by Pitts & Tayler (1989, 1996), Chamcham & Tayler

(1994). The effects of a generic inflow velocity profile on chemical evolution models has been explored by Lacey & Fall (1985), Tosi(1988), Götz & Köppen (1992), Köppen (1994), Edmunds & Greenhow (1995). A different approach is that of viscous disc models which, rather than imposing arbitrary radial velocity patterns, describe the evolution of the gas distribution in the disc self-consistently, following the model suggested by Lin & Pringle (1987). Viscous chemical models have been developed by Clarke (1989), Yoshii & Sommer-Larsen (1989) and Sommer-Larsen & Yoshii (1990), Thon & Meusinger (1998). All these studies show how radial inflows can steepen the metallicity gradients with respect to static models, especially if an outer cut-off of SF is assumed.

### 3. Modelling radial flows

We formulate our chemical model with radial flows as a multi-dimensional extension of the static model of PCB98 and PC99, an open model where the disc forms gradually by accretion of protogalactic gas. The disc is divided in  $N$  concentric rings or shells; in each ring  $k$  the gaseous component and its chemical abundances evolve due to:

1. depletion by SF, which locks up gas into stars;
2. stellar ejecta which shed back enriched material to the interstellar medium (ISM);
3. infall of primordial protogalactic gas;
4. gas exchange with the neighbouring rings because of radial flows.

The set of equations driving the chemical evolution of the  $k$ -th shell is:

$$\begin{aligned} \frac{d}{dt}G_i(r_k, t) = & -X_i(r_k, t)\Psi(r_k, t) + \\ & + \int_{M_i}^{M_u} \Psi(r_k, t - \tau_M) R_i(M)\Phi(M)dM + \\ & + \left[\frac{d}{dt}G_i(r_k, t)\right]_{inf} + \\ & + \left[\frac{d}{dt}G_i(r_k, t)\right]_{rf} \end{aligned} \quad (1)$$

where the various symbols are defined here below.

Primordial gas is accreted at an exponentially decreasing rate with time-scale  $\tau$ :

$$\dot{\sigma}_{inf}(r_k, t) = A(r_k) e^{-\frac{t}{\tau(r_k)}} \quad (2)$$

$A(r_k)$  is obtained by imposing that the integrated contribution of infall up to the present Galactic age  $t_G = 15$  Gyr, corresponds to an assumed exponential profile  $\sigma_A(r_k)$ :

$$A(r_k) = \frac{\sigma_A(r_k)}{\tau(r_k)(1 - e^{-t_G/\tau(r_k)})} = \frac{\sigma_A(r_\odot) e^{-\frac{r_k - r_\odot}{\tau_d}}}{\tau(r_k)(1 - e^{-t_G/\tau(r_k)})} \quad (3)$$

Indicating with  $\sigma_g(r_k, t)$  the surface gas density, we define the gas fraction:

$$G(r_k, t) = \frac{\sigma_g(r_k, t)}{\sigma_A(r_k)} \quad (4)$$

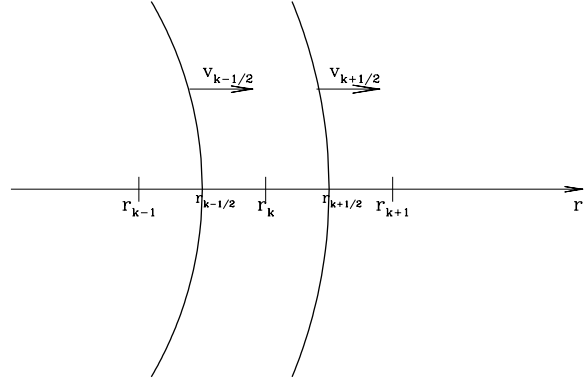


**Fig. 1.** Scheme of the gas flow through the  $k$ -th model shell

and the normalized surface gas density for each chemical species  $i$ :

$$G_i(r_k, t) = X_i(r_k, t) G(r_k, t) \quad (5)$$

where  $X_i$  is the fractionary abundance by mass of  $i$ .

The 1<sup>st</sup> term on the right-hand side of Eq. (1) represents the depletion of species  $i$  from the ISM due to star formation; see PC99 for the various options concerning the SF rate,  $\Psi(r, t)$ . The 2<sup>nd</sup> term is the amount of species  $i$  ejected back to the ISM by dying stars; the returned fractions  $R_i(M)$  are calculated on the base of the detailed stellar yields from PCB98 and keep track of finite stellar lifetimes (no instantaneous recycling approximation IRA). The 3<sup>rd</sup> term is the contribution of infall, while the 4<sup>th</sup> term describes the effect of radial flows. Full details on the first three terms can be found in the original static model by PCB98 and PC99. The novelty in Eq. (1) is the radial flow term, which we develop here below. We will adopt the simplified notation  $\sigma_{gk} \equiv \sigma_g(r_k, t)$  and the like.

Let the  $k$ -th shell be defined by the galactocentric radius  $r_k$ , its inner and outer edge being labelled as  $r_{k-\frac{1}{2}}$  and  $r_{k+\frac{1}{2}}$ . Through these edges, gas flows with velocity  $v_{k-\frac{1}{2}}$  and  $v_{k+\frac{1}{2}}$ , respectively (Fig. 1). Flow velocities are taken positive outward; the case of inflow is correspondingly described by negative velocities. Radial flows through the borders, with a flux  $F(r)$ , contribute to alter the gas surface density in the  $k$ -th shell according to:

$$\left[\frac{d\sigma_{gk}}{dt}\right]_{rf} = -\frac{1}{\pi(r_{k+\frac{1}{2}}^2 - r_{k-\frac{1}{2}}^2)} \left[F(r_{k+\frac{1}{2}}) - F(r_{k-\frac{1}{2}})\right] \quad (6)$$

The gas flux at  $r_{k+\frac{1}{2}}$  can be written:

$$F(r_{k+\frac{1}{2}}) = 2\pi r_{k+\frac{1}{2}} v_{k+\frac{1}{2}} \left[\chi(v_{k+\frac{1}{2}}) \sigma_{gk} + \chi(-v_{k+\frac{1}{2}}) \sigma_{g(k+1)}\right] \quad (7)$$

where  $\chi(x)$  is the step function:  $\chi(x) = 1$  or  $0$  for  $x >$  or  $\leq 0$ , respectively. Eq. (7) is a sort of ‘‘upwind approximation’’ for the advection term to be included in the

model equations (e.g. Press et al. 1986), describing either inflow or outflow depending on the sign of  $v_{k+\frac{1}{2}}$ . An analogous expression holds for  $F(r_{k-\frac{1}{2}})$ .

Let's take the inner edge  $r_{k-\frac{1}{2}}$  at the midpoint between  $r_{k-1}$  and  $r_k$ , and similarly for  $r_{k+\frac{1}{2}}$  (Fig. 1). Writing Eq. (6) separately for each chemical species  $i$ , in terms of the  $G_i$ 's we obtain the radial flow term of Eq. (1) as:

$$\left[\frac{d}{dt}G_i(r_k, t)\right]_{rf} = \alpha_k G_i(r_{k-1}, t) - \beta_k G_i(r_k, t) + \gamma_k G_i(r_{k+1}, t) \quad (8)$$

where:

$$\begin{aligned} \alpha_k &= \frac{2}{r_k + \frac{r_{k-1} + r_{k+1}}{2}} \left[ \chi(v_{k-\frac{1}{2}}) v_{k-\frac{1}{2}} \frac{r_{k-1} + r_k}{r_{k+1} - r_{k-1}} \right] \frac{\sigma_{A(k-1)}}{\sigma_{Ak}} \\ \beta_k &= -\frac{2}{r_k + \frac{r_{k-1} + r_{k+1}}{2}} \times \\ &\times \left[ \chi(-v_{k-\frac{1}{2}}) v_{k-\frac{1}{2}} \frac{r_{k-1} + r_k}{r_{k+1} + r_{k-1}} - \chi(v_{k+\frac{1}{2}}) v_{k+\frac{1}{2}} \frac{r_k + r_{k+1}}{r_{k+1} - r_{k-1}} \right] \quad (9) \\ \gamma_k &= -\frac{2}{r_k + \frac{r_{k-1} + r_{k+1}}{2}} \left[ \chi(-v_{k+\frac{1}{2}}) v_{k+\frac{1}{2}} \frac{r_k + r_{k+1}}{r_{k+1} - r_{k-1}} \right] \frac{\sigma_{A(k+1)}}{\sigma_{Ak}} \end{aligned}$$

The terms on the right-hand side of Eq. (8) evidence the contribution of the 3 contiguous shells involved: the first term represents the gas being gained in shell  $k$  from  $k-1$ , the second term is the gas being lost from  $k$  to  $k-1$  and  $k+1$ , and the third term is the gas being gained in  $k$  from  $k+1$ . The coefficients (9) are all  $\geq 0$  and depend only on the shell  $k$ , not on the chemical species  $i$  considered. If the velocity pattern is constant in time,  $\alpha_k$ ,  $\beta_k$  and  $\gamma_k$  are also constant in time.

Notice that in the case of static models the final surface mass density is completely determined by the assumed accretion profile, namely  $\sigma(r_k, t_G) \equiv \sigma_A(r_k)$ . Therefore, in static models the radial profile for accretion can be directly chosen so as to match the observed present-day surface density in the Disc (see PCB98 and PC99). The inclusion of the term of radial gas flows alters the expected final density profile and  $\sigma(r_k, t_G) \neq \sigma_A(r_k)$ . Hence,  $\sigma(r, t_G)$  cannot be assumed in advance and is only known *a posteriori* (see §4); at the end of each simulation we need to check how much radial flows have altered the actual density profile  $\sigma(r_k, t_G)$  with respect to the pure accretion profile  $\sigma_A(r_k)$ . With the slow flow speeds considered ( $v \lesssim 1 \text{ km sec}^{-1}$ ), the two profiles will not be too dissimilar anyways.

### 3.1. Boundary conditions

Eq. (8) needs to be slightly modified in the case of the innermost and the outermost shell, since the shell  $k-1$  or  $k+1$  are not defined in these two respective cases.

#### 3.1.1. The innermost shell

Our disc models will extend down to where the Bulge becomes the dominating Galactic component ( $r_1 = 2.5 \text{ kpc}$ ).

As to the innermost edge, we assume that the first shell is symmetric with respect to  $r_1$ :

$$r_{\frac{1}{2}} = \frac{3r_1 - r_2}{2}$$

and that  $v_{\frac{1}{2}} \leq 0$  always, since we cannot account for outflows from still inner shells, not included in the model. For  $k = 1$ , Eq. (8) then becomes:

$$\left[\frac{d}{dt}G_i(r_1, t)\right]_{rf} = -\beta_1 G_i(r_1, t) + \gamma_1 G_i(r_2, t) \quad (10)$$

with:

$$\begin{aligned} \beta_1 &= -\frac{1}{2r_1} \left[ v_{\frac{1}{2}} \frac{3r_1 - r_2}{r_2 - r_1} - \chi(v_{\frac{3}{2}}) v_{\frac{3}{2}} \frac{r_1 + r_2}{r_2 - r_1} \right] \\ \gamma_1 &= -\chi(-v_{\frac{3}{2}}) v_{\frac{3}{2}} \frac{1}{2r_1} \frac{r_1 + r_2}{r_2 - r_1} \frac{\sigma_{A2}}{\sigma_{A1}} \quad (11) \end{aligned}$$

#### 3.1.2. Boundary conditions at the disc edge

As to the outermost shell ( $k = N$ ), we need a boundary condition for the gas inflowing from the outer disc. We assume a SF cut-off in the outer disc, while the gaseous layer extends much further. In fact, in external spirals HI discs are observed to extend much beyond the optical disc, out to 2 or even 3 optical radii. A threshold preventing SF beyond a certain radius is expected from gravitational stability in fluid discs (Toomre 1964, Quirk 1972) and has observational support as well (Kennicutt 1989). For the Galactic Disc we assume no SF beyond the last shell at  $r_N = 20 \text{ kpc}$ , which is the empirical limit for the optical disc and for HII regions and bright blue stars tracing active SF. Gas can though flow in from the outer disc; extended gas discs might actually provide a much larger gas reservoir for star-forming spirals than vertical infall, at least at the present time when the gravitational settling of the protogalactic cloud is basically over.

If no SF occurs in the outer disc, the evolution of the gas (and total) surface density can be expressed as:

$$\frac{\partial \sigma}{\partial t}(r, t) = A(r) e^{-\frac{t}{\tau(r)}} - \frac{1}{r} \frac{\partial}{\partial r}(rv\sigma) \quad \forall r > r_{N+\frac{1}{2}} \quad (12)$$

(e.g. Lacey & Fall 1985, their model equation with the SF term dropped). Here, with no SF,  $\sigma \equiv \sigma_g$  and abundances always remain the primordial ones ( $X_{i,inf}$ ). Let's assume the following simplifying conditions for the outer disc:

1. the infall time-scale is uniform:

$$\tau(r) \equiv \tau(r_N) \quad \forall r > r_{N+\frac{1}{2}}$$

2. the inflow velocity is uniform and constant:

$$v(r, t) \equiv v_{N+\frac{1}{2}} \quad \forall r > r_{N+\frac{1}{2}}, \quad \forall t$$

3. the infall profile is flat:

$$A(r) \equiv A_{ext} \quad \forall r > r_{N+\frac{1}{2}}$$

in accordance with observed extended gas discs in spirals, showing a much longer scale-length than the stellar component.

With these assumptions, Eq. (12) becomes:

$$\frac{\partial \sigma}{\partial t} + v \frac{\partial \sigma}{\partial r} = A e^{-\frac{t}{\tau}} - \frac{v}{r} \sigma \quad (13)$$

where we indicate  $\tau \equiv \tau(r_N)$ ,  $v \equiv v_{N+\frac{1}{2}}$  and  $A \equiv A_{ext}$  to alleviate the notation. Eq. (13) has a straightforward analytical solution (Appendix B):

$$\begin{aligned} \sigma(r, t) &= A \tau \times \\ &\times \left[ \left( 1 - e^{-\frac{t}{\tau}} \right) + \frac{v}{r} \left( \tau \left( e^{-\frac{T_{rf}}{\tau}} - e^{-\frac{t}{\tau}} \right) - (t - T_{rf}) \right) \right] \end{aligned} \quad (14)$$

where  $T_{rf} \geq 0$  is the time when radial inflows are assumed to activate. Eq. (14) is our boundary condition at the outermost edge.

Notice that (14) is the solution of (13) in the idealized case of an infinite, flat gas layer extending boundless to any  $r > r_N$  (see also Appendix B). Of course, this does not correspond to gaseous discs surrounding real spirals; but since we will consider only slow inflow velocities ( $v \lesssim 1 \text{ km sec}^{-1}$ ), with typical values of  $r_N = 20 \text{ kpc}$  and  $t_G = 15 \text{ Gyr}$ , the gas actually drifting into the model disc shells will be just the gas originally accreted within  $r \sim 35 \text{ kpc}$ . Therefore, the boundary condition (14) remains valid as long as the gas layer stretches out to  $\sim 35 \text{ kpc}$ , a very plausible assumption since observed gaseous discs extend over a few tens or even  $\sim 100 \text{ kpc}$ .

### 3.1.3. The outermost shell

We take a reference external radius  $r_{ext} > r_N$  in the outer disc where the (total and gas) surface density  $\sigma(r_{ext}, t) \equiv \sigma_{ext}(t)$  is given by the boundary condition (14); typically,  $r_N = 20 \text{ kpc}$  and  $r_{ext} \sim 21 \text{ kpc}$ . We take the outer edge of the shell at the midpoint:

$$r_{N+\frac{1}{2}} = \frac{r_N + r_{ext}}{2}$$

and replace

$$X_{i(k+1)} \sigma_{g(k+1)} \longrightarrow X_{i,inf} \sigma_{ext}$$

in Eqs. (6) and (7), since the primordial abundances  $X_{i,inf}$  remain unaltered in the outer disc, in the absence of SF. We thus write the radial flow term for the  $N$ -th shell as:

$$\left[ \frac{d}{dt} G_i(r_N, t) \right]_{rf} = \alpha_N G_i(r_{N-1}, t) - \beta_N G_i(r_N, t) + \omega_i(t) \quad (15)$$

where:

$$\begin{aligned} \omega_i &= -X_{i,inf} \chi(-v_{N+\frac{1}{2}}) v_{N+\frac{1}{2}} \times \\ &\times \frac{4}{r_{N-1} + 2r_N + r_{ext}} \frac{r_N + r_{ext}}{r_{ext} - r_{N-1}} \frac{\sigma_{ext}(t)}{\sigma_{AN}} \end{aligned} \quad (16)$$

### 3.2. The numerical solution

Using (8), (10) and (15), the basic set of equations (1) can be written as:

$$\begin{cases} \frac{d}{dt} G_i(r_1, t) = \vartheta_1(t) G_i(r_1, t) + \gamma_1 G_i(r_2, t) + W_i(r_1, t) \\ \frac{d}{dt} G_i(r_k, t) = \alpha_k G_i(r_{k-1}, t) + \vartheta_k(t) G_i(r_k, t) + \\ \quad + \gamma_k G_i(r_k, t) + W_i(r_k, t) & k = 2, \dots, N-1 \\ \frac{d}{dt} G_i(r_N, t) = \alpha_N G_i(r_{N-1}, t) + \vartheta_N(t) G_i(r_N, t) + \\ \quad + W_i(r_N, t) + \omega_i(t) \end{cases}$$

where we have introduced:

$$\vartheta_k(t) \equiv -(\eta(r_k, t) + \beta_k) \leq 0$$

$$\eta(r_k, t) \equiv \frac{\Psi}{G}(r_k, t)$$

$$\begin{aligned} W_i(r_k, t) &\equiv \int_{M_i}^{M_u} \Psi(r_k, t - \tau_M) R_i(M) \Phi(M) dM + \\ &+ \left[ \frac{d}{dt} G_i(r_k, t) \right]_{inf} \end{aligned}$$

We refer to PCB98 for further details on the quantities  $\eta$  and  $W_i$ , appearing also in the original static model. Neglecting, for the time being, that the  $\eta$ 's and the  $W_i$ 's contain the  $G_i$ 's themselves, we are dealing with a linear, first order, non homogeneous system of differential equations with non constant coefficients, of the kind:

$$\frac{d\mathbf{G}_i}{dt} = \mathcal{A}(t) \mathbf{G}_i(t) + \mathbf{W}_i(t) \quad (17)$$

There is a system (17) for each chemical species  $i$ , but the matrix of the coefficients  $\mathcal{A}(t)$  is independent of  $i$ .

We solve the system by the same numerical method used for the original equation of the static model — see Talbot & Arnett (1971) and PCB98 for details. We just need to extend the method to the present multi-dimensional case (17). If we consider the evolution of the  $G_i$ 's over a short enough timestep  $t_1 - t_0 = \Delta t$ , the various quantities  $\eta(r_k, t)$ ,  $\vartheta_k(t)$  and  $W_i(r_k, t)$  will remain roughly constant within  $\Delta t$ ; similarly to the method for the static model (see PCB98), within  $\Delta t$  we approximate them with the values  $\bar{\eta}_k$ ,  $\bar{\vartheta}_k$  and  $\bar{W}_i(r_k)$  they assume at the midstep  $t_{\frac{1}{2}} = t_0 + \frac{1}{2} \Delta t$ . Over  $\Delta t$ , (17) can then be considered a system with constant coefficients  $\mathcal{A} \equiv \mathcal{A}(t_{\frac{1}{2}})$ , and  $\mathbf{W}_i(t)$  becomes a constant vector, which allows for the analytical solution:

$$\mathbf{G}_i(t_1) = e^{\Delta t \mathcal{A}} \mathbf{G}_i(t_0) + \left[ \int_{t_0}^{t_1} e^{(t_1-t)\mathcal{A}} dt \right] \mathbf{W}_i \quad (18)$$

where  $e^{t\mathcal{A}}$  indicates the matrix:

$$e^{t\mathcal{A}} = (e^{\lambda_1 t} \mathbf{u}_1 \quad \dots \quad e^{\lambda_N t} \mathbf{u}_N) (\mathbf{u}_1 \quad \dots \quad \mathbf{u}_N)^{-1} \quad (19)$$

with  $\lambda_k$  the eigenvalues of  $\mathcal{A}$  and  $\mathbf{u}_k$  the corresponding eigenvectors. The matrix  $e^{t\mathcal{A}}$  and the explicit expression

of the solution (18) for the  $G_i$ 's are calculated in Appendix A, resulting in:

$$\begin{aligned}
G_i(r_k, t_1) = & \alpha_k \times \\
& \times \frac{e^{-(\bar{\eta}_k + \beta_k)\Delta t} - e^{-(\bar{\eta}_{k-1} + \beta_{k-1})\Delta t}}{(\bar{\eta}_{k-1} + \beta_{k-1}) - (\bar{\eta}_k + \beta_k)} G_i(r_{k-1}, t_0) + \\
& + e^{-(\bar{\eta}_k + \beta_k)\Delta t} G_i(r_k, t_0) + \\
+ \gamma_k & \frac{e^{-(\bar{\eta}_{k+1} + \beta_{k+1})\Delta t} - e^{-(\bar{\eta}_k + \beta_k)\Delta t}}{(\bar{\eta}_k + \beta_k) - (\bar{\eta}_{k+1} + \beta_{k+1})} G_i(r_{k+1}, t_0) + \\
& + \alpha_k \frac{\bar{W}_i(r_{k-1})}{(\bar{\eta}_{k-1} + \beta_{k-1}) - (\bar{\eta}_k + \beta_k)} \times \\
& \times \left( \frac{1 - e^{-(\bar{\eta}_k + \beta_k)\Delta t}}{\bar{\eta}_k + \beta_k} - \frac{1 - e^{-(\bar{\eta}_{k-1} + \beta_{k-1})\Delta t}}{\bar{\eta}_{k-1} + \beta_{k-1}} \right) + \\
& + \bar{W}_i(r_k) \frac{1 - e^{-(\bar{\eta}_k + \beta_k)\Delta t}}{\bar{\eta}_k + \beta_k} + \\
+ \gamma_k & \frac{\bar{W}_i(r_{k+1})}{(\bar{\eta}_k + \beta_k) - (\bar{\eta}_{k+1} + \beta_{k+1})} \times \\
& \times \left( \frac{1 - e^{-(\bar{\eta}_{k+1} + \beta_{k+1})\Delta t}}{\bar{\eta}_{k+1} + \beta_{k+1}} - \frac{1 - e^{-(\bar{\eta}_k + \beta_k)\Delta t}}{\bar{\eta}_k + \beta_k} \right)
\end{aligned} \tag{20}$$

where we intend  $\alpha_1 \equiv 0$ ,  $\gamma_N \equiv 0$ , and for the outermost shell one should replace:

$$\bar{W}_i(r_N) \longrightarrow \bar{W}_i(r_N) + \bar{\omega}_i = \bar{W}_i(r_N) + \frac{1}{\Delta t} \int_{t_0}^{t_1} \omega_i(t) dt$$

$\omega_i$  being defined by (16).

Similarly to the case of an isolated shell (see PCB98) the system (20) does not provide the final solution for  $G_i(r_k, t_1)$ , since the  $\bar{\eta}_k$ 's and the  $\bar{W}_i$ 's on the right-hand side actually depend on the  $G_i$ 's; it just represents a set of implicit non-linear expressions in  $G_i(r_k, t_1)$ . As in the original static model, we can neglect the dependence of  $\bar{W}_i(r_k)$  on the  $G_i$ 's and consider only that of  $\bar{\eta}_k$  (see PCB98 for a detailed discussion). We must finally find the roots of the system (20) by applying the Newton-Raphson method, generalized to many dimensions (cfr. Press et al., 1986). Such a system holds for each of the chemical species  $i$  considered, so at each iteration we actually need to solve as many systems as the species included in the model. Full details on the mathematical development of the model and its numerical solution can be found in the appendices and in Portinari (1998).

We tested the code against suitable analytical counterparts and obtained the following conditions for model consistency (Appendix B).

1. Rather small timesteps are needed for the numerical model to keep stable; the required timesteps get smaller and smaller the higher the flow velocities considered, and the thinner the shells.
2. To describe gas flows in a disc with an exponential density profile, the shells should be equispaced in the logarithmic, rather than linear, scale (so that they roughly have the same mass, rather than the same width).

We modelled the Galactic Disc using 35 shells from 2.5 to 20 kpc, equally spaced in the logarithmic scale, their width ranging from  $\sim 0.2$  kpc for the inner shells to  $\sim 1$  kpc for the outermost ones. With such a grid spacing, and velocities up to  $\sim 1$  km sec $^{-1}$ , suitable timesteps are of  $10^{-4}$  Gyr (Appendix B; see also Thon & Meusinger

1998). This means that roughly  $1.5 \times 10^5$  timesteps, times 35 shells, are needed to complete each model, which would translate in excessive computational times. This drawback was avoided by separating the time-scales in the code.

1. The timestep  $\Delta t$  used to update the ‘‘chemical’’ variables ( $\eta$ ,  $W_i$ , etc.) is the minimum among:  $\Delta t_1$  which guarantees that the relative variations of the  $G_i$ 's are lower than a fixed  $\epsilon$ ;  $\Delta t_2$  which guarantees that the total surface mass density  $\sigma(t)$  increases by no more than 5%;  $\Delta t_3$  which is twice the previous timestep of the model, to speed up the computation when possible;  $\Delta t_4$  which guarantees the Courant condition  $\Delta t < v \Delta r$ , indispensable for the stability of a numerical algorithm describing flows. So,  $\Delta t$  is basically set by the requirement that the chemical quantities do not vary too much within it, and it can get relatively large (up to 0.2 Gyr), especially at late ages when the various chemical variables evolve slowly.
2. It is only the numerical solution (20) which needs very short timesteps to keep stable. Therefore, once the chemical variables are upgraded, the main timestep  $\Delta t$  is subdivided in much shorter timesteps  $\delta t = 10^{-4}$  Gyr, upon which the solution (20) and its Newton-Raphson iteration are successively applied to cover the whole  $\Delta t$ . Only then a new upgrade of all the  $\bar{\eta}_k$ 's and  $\bar{W}_i$ 's is performed.

This trick keeps the code roughly as fast as if it would evolve with a single time-scale  $\Delta t$ , and yet it gives the same results as the ‘‘slow’’ version in which all quantities are upgraded at each  $\delta t = 10^{-4}$  Gyr.

**Table 1.** Parameter values and resulting metallicity gradients for models S15RF, O10RF and DRRF

model	$r_d$	$\nu$	$\zeta$	$\tau$	$v(r)$	$\frac{d[O/H]}{dr}$
S15a	4	0.35	0.2	3	0	-0.03
S15RFa	4	0.35	0.2	3	-1	-0.053
S15RFb	5	0.4	0.32	3	-1	-0.047
S15RFc	4	0.35	0.2	3	$\begin{cases} -1 \\ v_{N+\frac{1}{2}} = 0 \end{cases}$	-0.083
S15RFd	7	0.35	0.35	3	$\begin{cases} -1 \\ v_{N+\frac{1}{2}} = 0 \end{cases}$	-0.073
S15RFe	6	0.37	0.25	3	Fig. 4	-0.063
O10a	4	0.19	0.2	3	0	-0.03
O10RFe	7	0.2	0.25	3	Fig. 4	-0.07
DRa	4	0.42	0.2	3	0	-0.07 ( $r > r_\odot$ ) flat ( $r < r_\odot$ )
DRRFe	4	0.5	0.27	3	Fig. 7	-0.059

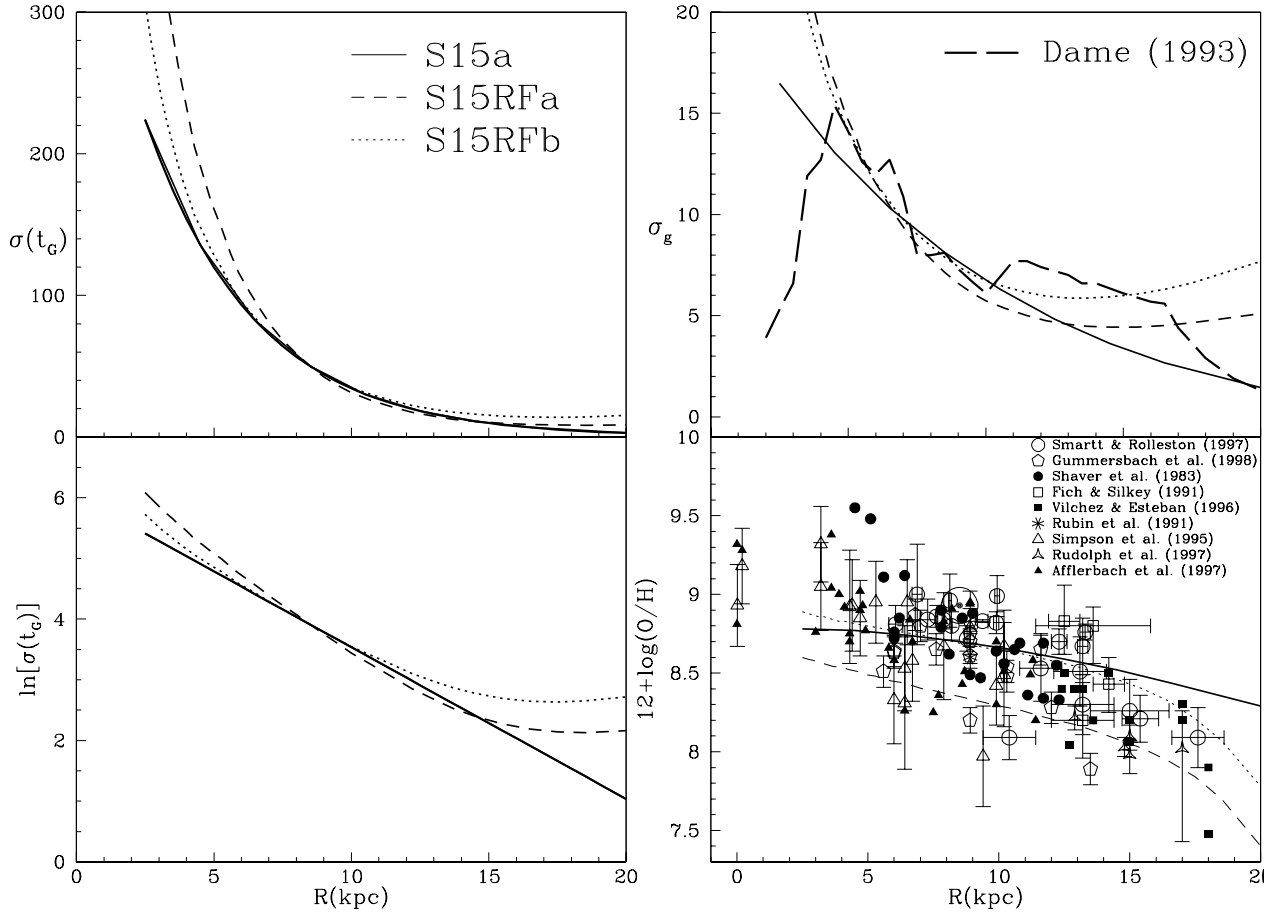


**Fig. 2.** *Left panels:* final profiles of the total surface density from models S15RF with inflow from the outer disc, in linear (upper panel) or logarithmic (lower panel) plot; the reference observed profile of models with scale length 4 kpc, as adopted in models with no flows (PC99), is shown as a thick solid line. *Upper right panel:* radial gas density profiles compared to the observed one. *Lower right panel:* predicted radial metallicity profiles compared to the observational data (data and symbols as in PC99).

#### 4. Effects of radial inflows on the disc

After presenting our new model with radial flows, we investigate their general effects on the chemical evolution of the disc. Here we first analyse how the predicted metallicity gradient and gas and total surface density profiles of a static model are altered by a superimposed uniform gas inflow, while in Section 5 we will suitably combine radial flows with various SF laws to match the observed radial profile of the Disc. The characteristics and parameters of the various models presented in this and in the next section are summarized in Table 1.

To gain a qualitative understanding of the effects of radial gas inflows on chemical evolution, we impose a uniform inflow pattern  $v = -1 \text{ km sec}^{-1}$  upon a static chemical model and compare the new outcome with the original static case. Radial flows over the disc are expected to be mainly inflows, with velocities from 0.1 to  $\sim 1 \text{ km sec}^{-1}$  (see §2); imposing a uniform inflow of  $1 \text{ km sec}^{-1}$  is there-

fore a sort of “extreme case”, considered here for the sake of qualitative analysis. Anyways, previous studies in literature suggest that the effects of radial flows saturate for much higher velocities (Köppen 1994). We will consider both the case of inflow from the outer gaseous disc and not ( $v_{N+\frac{1}{2}} = -1$  or 0, respectively).

All models with radial flows are rescaled so that the final surface density at the Solar ring ( $r_\odot = 8.5 \text{ kpc}$ ) corresponds to  $50 M_\odot \text{ pc}^{-2}$ . Namely, with radial flows  $\sigma(r_\odot, t_G) \neq \sigma_A(r_\odot)$  and it cannot be imposed as an input datum (see §3), but the zero-point  $A(r_\odot)$  of the exponential accretion profile (3)

$$A(r) = A(r_\odot) e^{-\frac{r-r_\odot}{r_d}}$$

can be rescaled so that at the end of the simulation  $\sigma(r_\odot, t_G) = 50 M_\odot \text{ pc}^{-2}$ . This zero-point does not influence the profile, nor the chemical evolution, so it can always be rescaled *a posteriori*.

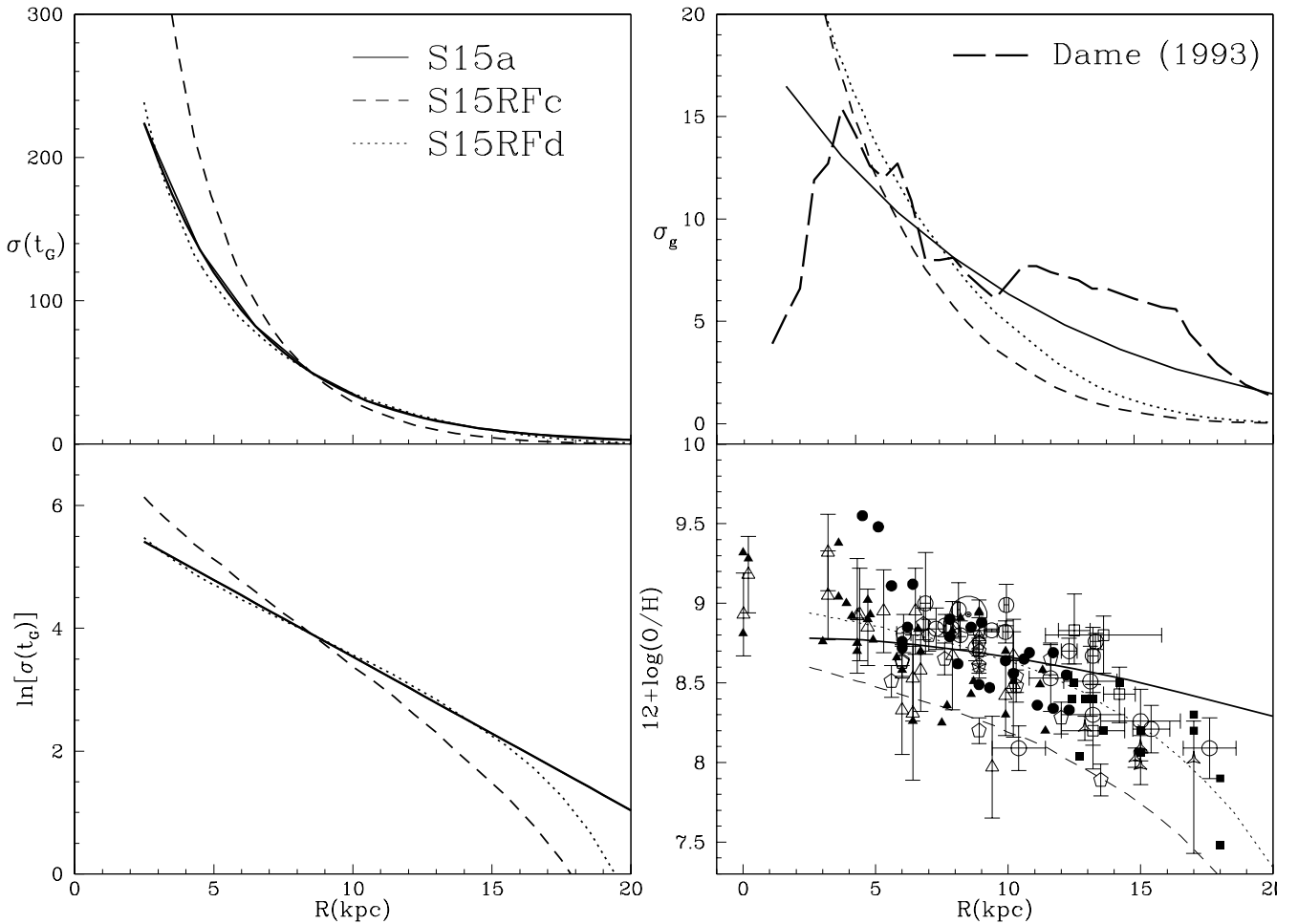


**Fig. 3.** Same as Fig. 2, but for models S15RF with no inflow from the outer disc edge.

For our example, we take as the reference static case a model adopting a Schmidt SF law with  $\kappa = 1.5$  (Kennicutt 1998) and a uniform infall time-scale of 3 Gyr (model S15a of PC99, see also Table 1).

#### 4.1. Models with inflow from the outer disc

In model S15RFa a uniform radial inflow pattern with  $v = -1 \text{ km sec}^{-1}$  and inflow from the outer disc is imposed upon the static model S15a, with no further change in the model parameters (Table 1). Fig. 2 shows the effects of inflow on the total surface density and gas density distribution, and on the oxygen gradient (details on the observational data in the plots can be found in PC99). By comparing the solid line and the dashed line, we notice the following main effects.

- Since matter flows inward and accumulates toward the Galactic Centre, the density profile gets steeper in the inner parts, while in the outer parts it remains rather flat because gas is continuously poured in by the flat

outer gaseous disc. The gas density distribution shows a similar behaviour.

- The overall metallicity gets much lower because of the dilution by primordial gas inflowing from the outer disc. The gradient becomes steeper, especially in the outermost shells, since the discontinuity in metallicity between the star-forming disc and the outer gaseous layer is smeared inward by radial inflows.

To compensate for the steepening of the density distribution induced by radial inflows, we must adopt a shallower initial accretion profile; our simulations show that a scale length  $r_d \sim 5 \text{ kpc}$  for the infall profile reduces in the end to a density profile matching the desired scale length of  $\sim 4 \text{ kpc}$  at the Solar Neighbourhood. At the same time, the chemical enrichment must get more efficient for the overall metallicity to increase to the observed levels; the predicted metallicity is improved by adopting an IMF more weighted towards massive stars, i.e. by increasing the “IMF scaling fraction”  $\zeta$  (see PCB98 and PC99 for a description of our model parameters). Together with the SF efficiency  $\nu$ ,  $\zeta$  is re-calibrated to match the observed gas surface density

and metallicity at the Solar Neighbourhood (as for the models of PC99). In this way we calibrate model S15RFb with respect to the Solar Neighbourhood; see Table 1 for details on the adopted parameters. Comparing now this re-calibrated model with radial flows (dotted line) to the original model S15a, the metallicity gradient is increased with respect to the static case, but still a bit flat with respect to observations. The gas density distribution peaks in the inner regions, as expected, and remains quite high (much higher than observed) in the outer regions due to substantial replenishment from the outer disc.

4.2. Models with no inflow from the outer disc

Let’s now consider the case when radial flows are limited within the star forming disc and there is no inflow from the external gaseous disc ( $v_{N+\frac{1}{2}} = 0$ ). If radial flows are mainly driven by shocks in spiral arms, for instance, they might indeed occur only within the stellar disc, while the outer gas layer remains unperturbed.

Fig. 3 (left panels) shows how the final density profile becomes much steeper than the reference accretion profile (model S15RFc, dashed line), as expected since matter is efficiently drifting inward with no replenishment from the outer disc. For the final density profile to match the observed one, we must assume a much shallower initial accretion profile ( $r_d \sim 6 - 7$  kpc). Then the resulting local density profile is close to the observed one, while in the outer parts the profile remains steeper (model S15RFd, dotted line).

The gas density profile shows a similar behaviour, strongly peaked toward the centre while dropping quickly (much more quickly than observed) outside the Solar ring (upper right panel).

The overall metallicity is reduced with respect to the original model S15a (lower right panel, model S15RFc) and again we need to increase the IMF scaling fraction  $\zeta$  to raise the chemical enrichment to the observed values (model S15RFd). The resulting gradient is roughly comparable to the observed one.

4.3. Concluding remarks

We can summarize the general effects of radial flows as follows.

- Since matter flows inward and accumulates toward the Galactic Centre, the density profile in the inner parts gets steeper. A shallower intrinsic accretion profile is to be adopted, in order to recover the observed local scale-length at the end of the simulation.
- In the outer parts, the profile declines more or less sharply, depending on whether the inflow occurs only within the star-forming disc or there is also substantial inflow from the outer, purely gaseous disc.

- The gas distribution shows a similar behaviour: it remains quite flat in the outer regions if gas is poured in by the flat outer gas disc, while it tends to drop sharply (more than observed) otherwise.
- The inner gas profile is very steep in the case of a Schmidt SF law (models S15RF) — while with other SF laws with radially decaying efficiency (see PC99 and §5) the effect would be somewhat compensated by a larger gas consumption by SF in the inner regions.
- The overall metallicity gets much lower because of the dilution by gas inflowing from metal poor outer shells (and possibly the primordial outer disc). A higher fraction of stars contributing to the chemical enrichment is needed in the model to match the observed metallicity.
- The metallicity gradient tends to steepen, in agreement with results by other authors (see references in §2).

5. Some “successful” models

In §4 we have illustrated the qualitative effects of radial inflows using, for the sake of example, models with a Schmidt SF law. We will now consider models with various SF laws (see PC99) and tune the inflow velocity pattern, in each case, so as to match the observational data on the radial profile of the Galactic Disc. The various “successful” models presented here should not be taken as detailed, unique recipes to reproduce the Disc. Rather, they are meant as examples of how inclusion of radial flows in the chemical model can improve the match with the data.

5.1. Models with Schmidt law

Let’s first consider again the Schmidt SF law. Inspection of models S15RFb and S15RFd (with and without radial inflows from the outer disc) suggests to proceed as follows.

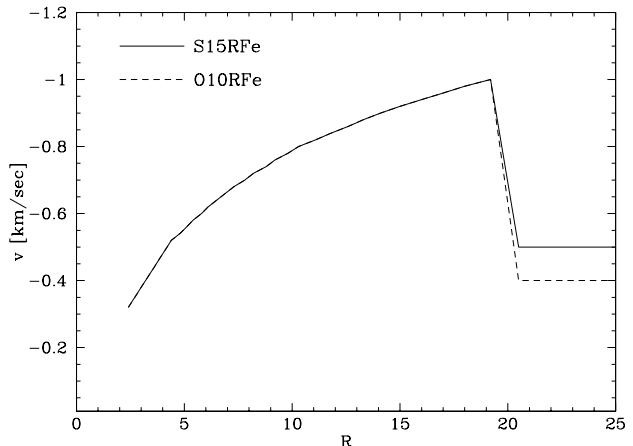
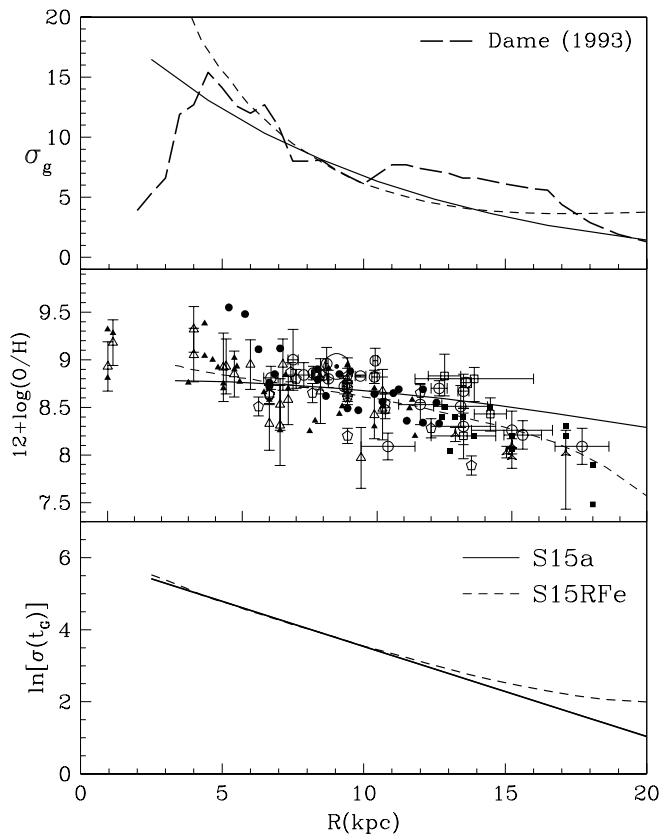
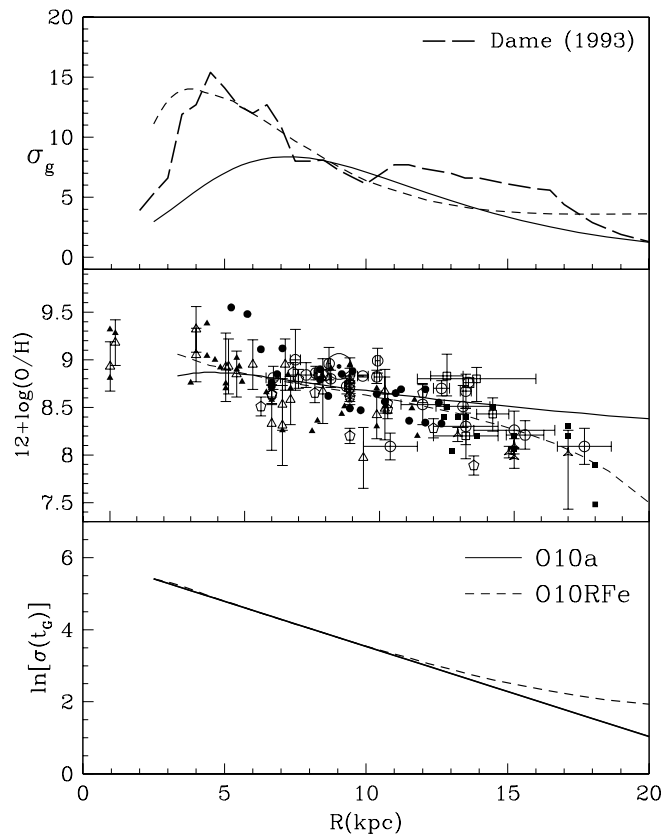


Fig. 4. Inflow velocity pattern for the “successful” models S15RFe and O10RFe.





**Fig. 5.** A “successful” S15RFe model compared to the case with no flows. Data and symbols as in Fig. 2.



**Fig. 6.** A “successful” O10RF model compared to the case with no flows.

- Some inflow from the outer gaseous layer is needed to reproduce the shallow decline of the gas distribution observed out of the Solar ring, though the inflow speed from the outer disc should be slower than  $-1 \text{ km sec}^{-1}$  otherwise the predicted gas density is too high in the outer parts (as in model S15RFb).
- Models with radial inflows can predict metallicity gradients close to the observed ones even with a Schmidt SF law, provided drift velocities within the star-forming edge are relatively high (of the order of  $-1 \text{ km sec}^{-1}$ ). Inflow patterns decelerating inward are particularly efficient in building the metallicity gradient (Götz & Köppen 1992).

An example of a drift velocity profile shaped according to these considerations is shown in Fig. 4; the corresponding model gives indeed a reasonable fit to the data (model S15RFe, Fig. 5). The gas profile keeps increasing inward, yet the model does not reproduce the peak of the molecular ring, for which we need to include the peculiar radial flows induced by the Bar (see the discussion in PC99 and §6). Model S15RFe shows how radial inflows can in fact allow for metallicity gradients comparable with the ob-

served ones, even with a Schmidt SF law which would be excluded on the sole base of static models (PC99).

### 5.2. Models with spiral-triggered SF laws

Let’s consider now models adopting an Oort-type SF law, with a SF efficiency inversely proportional to the galactocentric radius and a Schmidt-like exponent  $\kappa = 1.0$  (Kennicutt 1998, PC99). The static and the “successful” model with this SF law are model O10a from PC99 and model O10RFe, respectively (Table 1).

As in the static case, (see PC99), these models behave somewhat similarly to models adopting the Schmidt SF law. Fig. 6 shows that a good fit is obtained with model O10RFe, where we applied the velocity pattern of Fig. 4 with inflows becoming slower inward, very close to that used for model S15RFe. Notice that in this case the higher SF efficiency in the inner region and the slowdown of inflows conspire to accumulate gas around  $r = 3 \text{ kpc}$  while consuming it at inner radii, generating a peak in the predicted gas distribution which closely reminds the observed molecular ring.

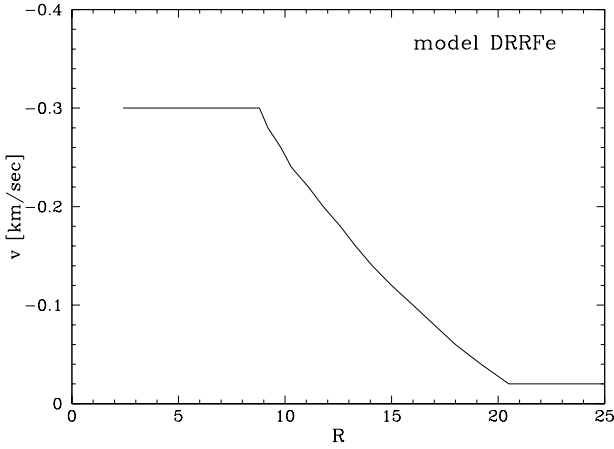


**Fig. 7.** Inflow velocity pattern for the “successful” model DRRF

### 5.3. Models with gravitational self-regulating SF laws

We now investigate models adopting a self-regulating SF process driven by gravitational settling and feed-back from massive stars, implying a SF efficiency exponentially decaying outward in radius, such as the law by Dopita & Ryder (1994; see PC99). The reference static model in this case is model DRa of PC99, while the corresponding “successful” model with radial flows is DRRFe (see Table 1 for the relevant parameters).

To reproduce the observed metallicity gradient with this SF law, negligible inflow is required in the outer regions where static models already predict a gradient with the right slope (see model DRa), while a moderate inflow velocity ( $\sim 0.3 \text{ km sec}^{-1}$ ) in the inner parts is needed to maintain the observed slope also where the predicted gradient would otherwise flatten (see PC99). Such a model is, for example, model DRRFe, obtained with the inflow velocity pattern shown in Fig. 7. In Fig. 8 the “successful” model DRRFe is compared to the original model DRa of PC99 with no radial flows.

### 5.4. Concluding remarks

The aim of the previous “successful” examples is to remark how, for each SF law considered, it is possible to tune the inflow velocity pattern so as to get a good overall agreement with the observational data. As an indication, suitable inflow profiles have the following characteristics.

- With a Schmidt SF law, relatively fast (but still plausible) flows are needed within the star-forming disc, with velocities of the order of  $1 \text{ km sec}^{-1}$ . The required metallicity gradient is easily obtained, especially if the inflow velocity is slowly decreasing inward.

Inflow from the outer gaseous disc must be less prominent (though present), otherwise the predicted gas density in the outer regions is too high.

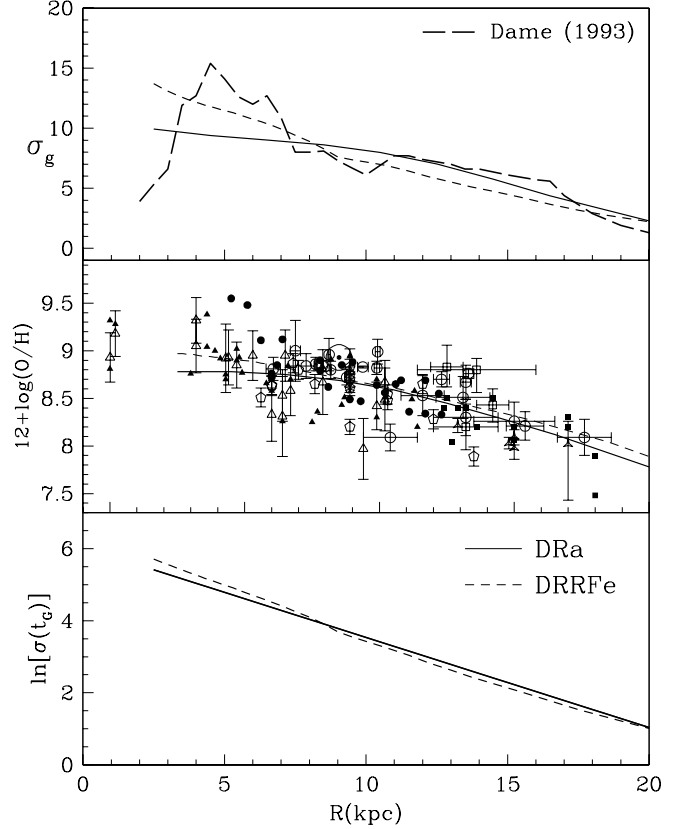


**Fig. 8.** A “successful” DRRF model compared to the case with no flows.

- In models adopting an Oort-type SF law with  $\kappa = 1.0$ , a good fit to the data is obtained with an inflow profile of the same kind: inflow at  $\sim 0.5 \text{ km sec}^{-1}$  from the outer gaseous disc, drift velocities raising at  $\sim 1 \text{ km sec}^{-1}$  at the stellar disc edge and declining inward. Curiously enough, in this case the higher SF efficiency in the inner regions combines with the slow-down of inflows to predict a peak in the gas distribution around  $r = 3 \text{ kpc}$ , quite reminiscent of the observed molecular ring.
- Models adopting the SF law by Dopita & Ryder give a good description of the outer regions of the Disc already in the absence of flows (PC99). Mild radial inflows can be assumed in the inner regions, where the radial gradient would otherwise flatten, to obtain the right slope throughout the disc. The required drift velocities are around  $0.3 \text{ km sec}^{-1}$ , which can be reasonably provided, for instance, by the shocks occurring within the spiral arms (see §2).

The various “successful models” presented here are not meant to be definitive recipes to reproduce the radial profile of the Galactic Disc. In fact, the adopted inflow velocity profiles are quite arbitrary and *ad hoc*. These models

are rather meant to show how radial flows can be a viable mechanism to interpret the properties of the Disc. In PC99 we showed how none of the various SF laws investigated is able, by itself, to reproduce the observed metallicity gradient throughout the whole extent of the Disc, unless some additional “dynamical” assumption is included. In PC99 we considered the classical case of an inside–out disc formation, namely of an infall time-scale increasing outward. Here, we just show that radial inflows can provide another viable “dynamical” assumption to be combined with any SF law to reproduce the observed gradient. In particular, if we adopt a Schmidt SF law with  $\kappa = 1.5$  or an Oort–type SF law with  $\kappa = 1.0$ , as recent empirical evidence seems to support (Kennicutt 1998), the required variation of the accretion time-scale is too extreme in the pure inside–out assumption (PC99), and radial inflows are then necessary to explain the metallicity gradient. Of course, the two effects (inside–out formation and radial flows) can also play at the same time. We do not address here their combined outcome, because in our models this would merely translate into increasing the number of parameters which one can tune to fit the observational data. No further insight in the problem would be gained. With this kind of models we can just learn how the various players (different SF laws, radially varying accretion time-scales, radial gas inflows) enter the game of reconstructing the general picture, and analyse their effects one by one.

It is also worth stressing that even slow radial gas flows, with velocities well plausible in terms of the triggering physical mechanisms and within the observational limits (§2), have non–negligible influence on chemical models, especially on the gas density distribution. It is therefore misleading to seek for a one–to–one relation between gas content and metallicity, or between gas profile and metallicity gradient, like the one predicted by simple models (e.g. Tinsley 1980). When studying the chemical features of galaxies, it is very dangerous to assume that such a relation must hold, since even mild flows can easily alter the overall distribution.

The models with smooth radial inflows presented in this section (with the possible exception of model O10RFe) are still unable to reproduce the gas density peak corresponding to the molecular ring around 4 kpc, since that needs to take into account the peculiar dynamical influence of the Galactic Bar on gas flows. This will be the issue of the next section.

## 6. The role of the Galactic Bar

There is by now substantial evidence that the Milky Way hosts a small Bar in its inner 3 kpc or so. The idea was originally suggested to explain the kinematics of the atomic and molecular gas near the Galactic Centre (de Vaucouleurs 1964, Peters 1975, Liszt & Burton 1980, Mulder & Liem 1986). In recent years further evidence for a Galactic Bar has piled up from several tracers: gas

dynamics (Binney et al. 1991; Weiner & Sellwood 1996, 1999; Yuan 1993; Wada et al. 1994; Englmaier & Gerhard 1999; Fux 1999), IR photometry and star counts (Blitz & Spergel 1991, Weinberg 1992, Nikolaev & Weinberg 1997, Dwek et al. 1995, Binney et al. 1997, Unavane & Gilmore 1998), stellar kinematics (Zhao et al. 1994; Weinberg 1994; Fux 1997; Sevenster 1997, 1999; Sevenster et al. 1999; Raboud et al. 1998), OGLE data (Stanek et al. 1994, 1997; Paczynski et al. 1994; Evans 1994; Zhao et al. 1995, 1996; Zhao & De Zeeuw 1998, Ng et al. 1996). For a review on the Galactic Bar see e.g. Gerhard (1996, 1999). The determination of the characteristic parameters (size, axis ratio, rotation speed, orientation and so forth) is even more difficult for the Bar of our own Milky Way than for external galaxies. Broadly speaking, the various studies mentioned above indicate a Bar with a major axis of 2–4 kpc viewed at an angle of 15–45° in the first longitude quadrant, an axis ratio around 3:1 and a pattern speed  $\Omega_p \sim 60 \text{ km sec}^{-1} \text{ kpc}^{-1}$ .

PC99 underlined that the dynamical influence of the Galactic Bar is likely to account for the peak at 4 kpc displayed by the gas profile in the Disc, which static chemical models are unable to reproduce if other constraints, like the observed metallicity gradient, are to be matched as well. In fact, gravitational torques in a barred, or non–axisymmetric, potential are thought to induce gas accumulation and formation of rings at the corresponding Lindblad resonances (e.g. Combes & Gerin 1985; Schwarz 1981, 1984). In brief, bar–induced flows sweep gas away from the co–rotation (CR) radius, where the bar roughly ends, toward the inner and outer Lindblad resonances (ILR, OLR). In fact, we developed our new chemical model with radial flows also with the aim to mimic such effects of the Bar upon the gas distribution, by simulating suitable flow velocity profiles.

As mentioned above, though the existence and gross features of the Galactic Bar are by now established, there is no general agreement on details like its size and pattern speed, and on the corresponding radii for its CR and ILR, OLR. In this paper, with the aim to reproduce the molecular ring at 4–6 kpc, we will consider two Bar models covering the range of scenarios suggested in literature:

**case A)** Bar’s CR around 3.5 kpc, so that the dip in the gas distribution between 1.5 and 3.5 kpc is interpreted as a fast inward drift of gas from CR to the ILR and the nuclear ring;

**case B)** Bar’s CR around 2.5 kpc and OLR around 4.5 kpc, so that the molecular ring is interpreted as accumulation of gas from CR toward the OLR.

In any case, we will assume here that the Bar influences only the inner 5–6 kpc of the Galactic Disc, where its OLR is supposed to lie at the outermost according to current understanding, while leaving regions outside the OLR unaffected (see also Gerhard 1999). Actually, the possible influence of the Bar over a larger Disc region than its for-

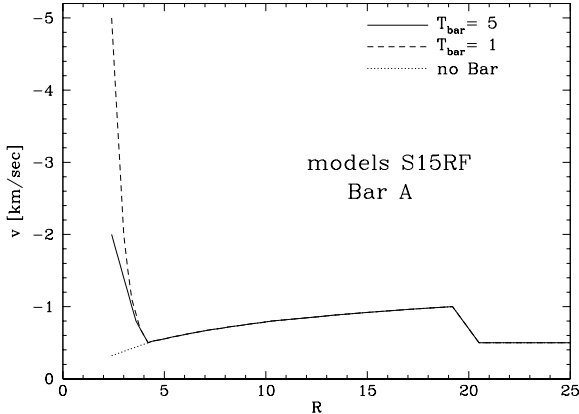


**Fig. 9.** Inflow velocity pattern adopted from the onset of the Bar at the time  $t_G - T_{bar}$  upon the base “no Bar” model (S15RFe), to mimic case A for the Galactic Bar with models S15RF. The dotted line applies to the base model S15RFe, and also to the “barred” models before  $t_G - T_{bar}$ .

mal extent is still an open problem, as we will comment upon in the final conclusions (§7).

In the framework of our chemical model, the inclusion of the Bar translates into imposing a suitable velocity profile for the radial flows in the inner regions of the disc. Namely, we run the “successful models” with radial flows presented in §5, but at a suitable age the Bar is assumed to form and the radial velocity profile is altered correspondingly, by modifying the coefficients  $\alpha_k$ ,  $\beta_k$ ,  $\gamma_k$  describing the radial flow pattern (§3). In case A, we will impose fast radial inflow velocities within CR at 3–4 kpc to mimic the rapid drift of the gas toward the ILR (§6.1). In case B, we will impose outflows from CR to the OLR around 4.5 kpc (§6.2).

As to the age of the Bar, an upper limit is set by the typical age of its stellar population, 8–9 Gyr (Ng et al. 1996); an age of 5 to 8 Gyr has been suggested by Sevenster (1997, 1999). The results from our simulations turned out to be quite insensitive to a change in the Bar’s age from 9 to 5 Gyr; therefore, we will present simulations with a 5 Gyr old Bar ( $T_{bar} = 5$ ) as representative of the generic case of age  $\gtrsim 5$  Gyr. We will also consider, for the sake of completeness, the case of a much younger Bar of 1 Gyr of age ( $T_{bar} = 1$ ).

### 6.1. Modelling the effects of the Bar: case A

To mimic case A, where the Bar induces fast inflows from CR to its ILR, the inflow velocity is typically increased for  $r < 3.5 - 4$  kpc (the Bar’s CR radius) with respect to the drift pattern adopted before the onset of the Bar. Models corresponding to case A give good results when combined with a Schmidt SF law with radial inflows. Starting from the corresponding “successful” model S15RFe of §5

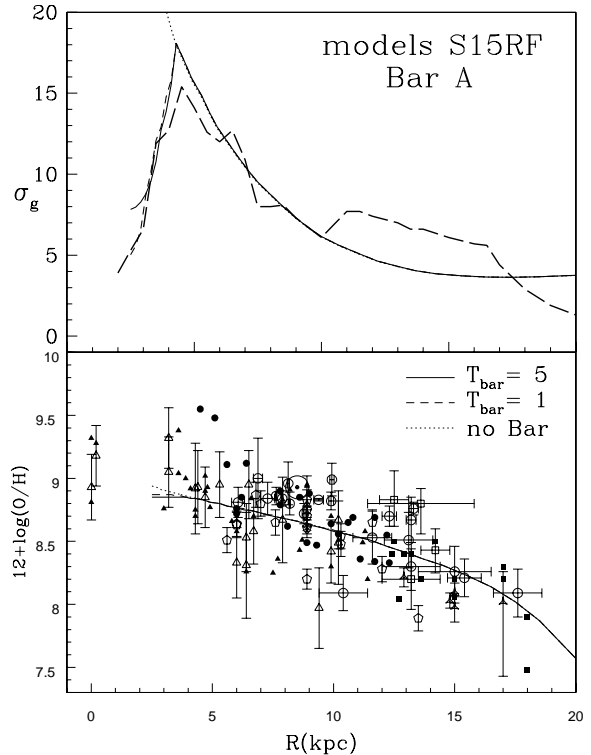


**Fig. 10.** Models S15RF mimicking case A for the Galactic Bar, adopting the inflow patterns of Fig. 9. The “no Bar” model S15RFe is also shown for comparison as a dotted line.

and changing the velocity law as in Fig. 9 at the onset of the Bar, we obtained the models shown in Fig. 10, compared to the original model S15RFe with no Bar’s effects included. Obviously, if the Bar is younger ( $T_{bar} = 1$  Gyr) faster induced inflows need to be assumed in the inner regions so that the observed sharp dip in the gas profile at  $r \lesssim 3.5$  kpc is obtained in a shorter time (Fig. 9). Anyway, no extreme speeds need to be induced by the Bar ( $|v| < 5$  km sec) at these radii yet, to resemble the observed gas profile, so the models remain plausible.

This type of solution actually corresponds to the one originally suggested by Lacey & Fall (1985), who in fact assumed a Schmidt SF law, radial inflows of the order of  $-1$  km sec $^{-1}$  to reproduce the metallicity gradient, and for  $r \leq 4$  kpc a raise in the inflow speed up to  $-10$  km sec $^{-1}$  to reproduce the gas profile. Without such a spike in the inflow velocity, the gas distribution keeps rising inward, with no depression (cfr. model S15RFe). This picture also corresponds to the situation for viscous models as suggested by Thon & Meusinger (1998): the detailed gas profile of the Disc can be reproduced only by artificially increasing the viscosity in the inner regions, so as to mimic the influence of the Galactic Bar.

Case A can also well combine with model O10RFe, namely with an Oort-type SF law with  $\kappa = 1$  plus the

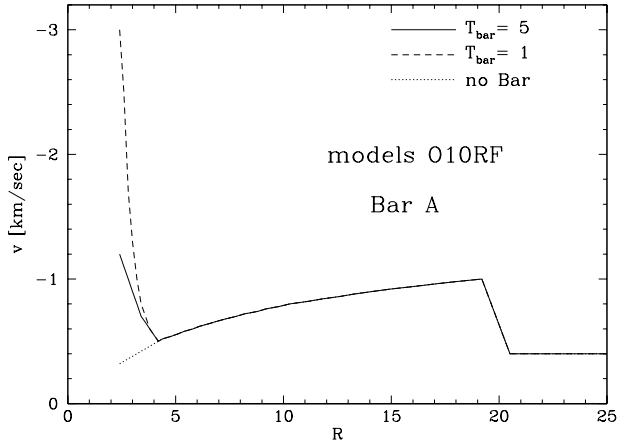


**Fig. 11.** Inflow velocity pattern adopted from  $t_G - T_{bar}$  upon the base (“no Bar”) model O10RFe, to mimic case A for the Galactic Bar with models O10RF.

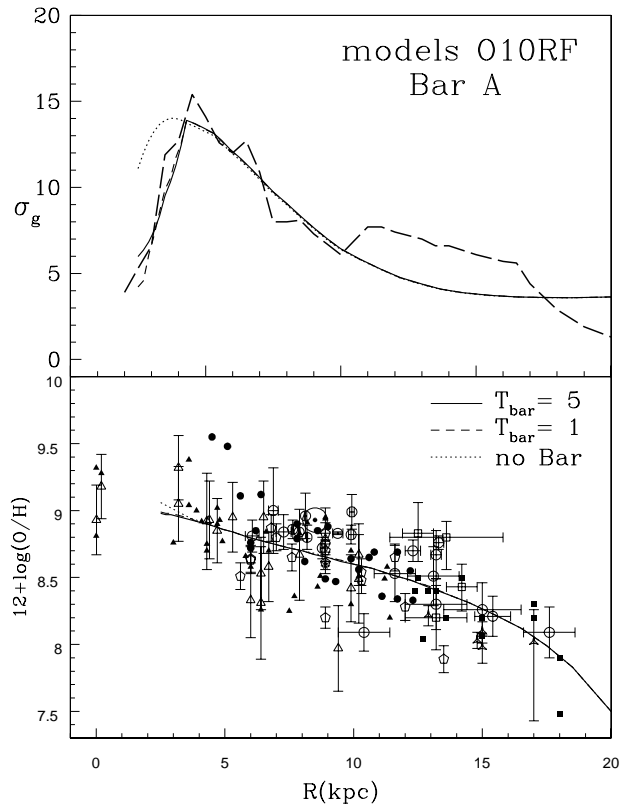


**Fig. 12.** Models O10RF mimicking case A for the Galactic Bar, adopting the inflow patterns of Fig. 11.

corresponding “successful” inflow pattern. In fact, also in model O10RFe (which is actually the only model able to predict a peak in the gas profile reminding of the molecular ring even without including the Bar, see §5) the gas profile rises inward, and by increasing the inflow velocities

inside 4 kpc one can fit the observed gas depression. As an example, we show models O10RF with inflow patterns as in Fig. 11; the corresponding results are plotted in Fig. 12 together with the base model O10RFe.

Notice how in all these “case A” models the metallicity gradient is only negligibly affected by the switch of the inner inflow pattern at the time of onset of the Bar,  $t_G - T_{bar}$  ( $t_G = 15$  Gyr is the present Galactic age). The effects are at most limited to  $r \lesssim 3$  kpc, where they are hard to check from observations, since in that region the gas distribution is depressed and the metallicity tracers are missing as well, since they are young objects strongly correlated to present-day SF activity and therefore to the presence of gas. We remark that abundance data at  $r = 0$  in the plots for the abundance gradient are to be disregarded as a constraint for the model, since they refer to the Galactic Centre population, not to the Disc (see PC99).

### 6.2. Modelling the effects of the Bar: case B

According to what we labelled above as “case B”, the Galactic Bar ends in correspondence to its CR around 2.5 kpc, and it has an OLR around 4.5 kpc. Therefore, the gas is expected to drift from CR outward and accumulate at the OLR, while gas inflowing from outer regions slows down and accumulates as well at the level of the resonance at 4.5 kpc.

Models for case B will adopt, starting from  $t_G - T_{bar}$ , a radial flow pattern with positive velocities (outflow) from  $r = 2.5$  kpc to  $r \sim 4.5$  kpc, and negative velocities (inflow) from outside dropping to zero at  $r \sim 4.5$  kpc. Case B can be combined with model DRRFe, namely with the SF law by Dopita & Ryder (1994) and the corresponding “success-

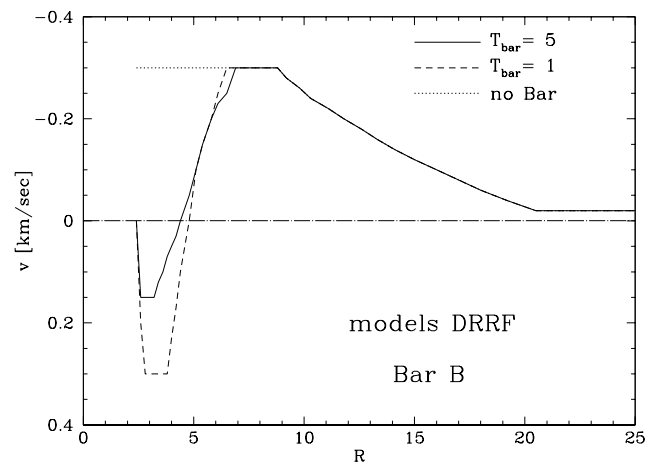


**Fig. 13.** Radial flow velocity pattern adopted from  $t_G - T_{bar}$  upon the base “no Bar” inflow pattern, to mimic case B for the Galactic Bar with models DRRF. The dot-dashed horizontal line at  $v = 0$  marks the transition from inflows (negative  $v$ ) to outflows (positive  $v$ ).

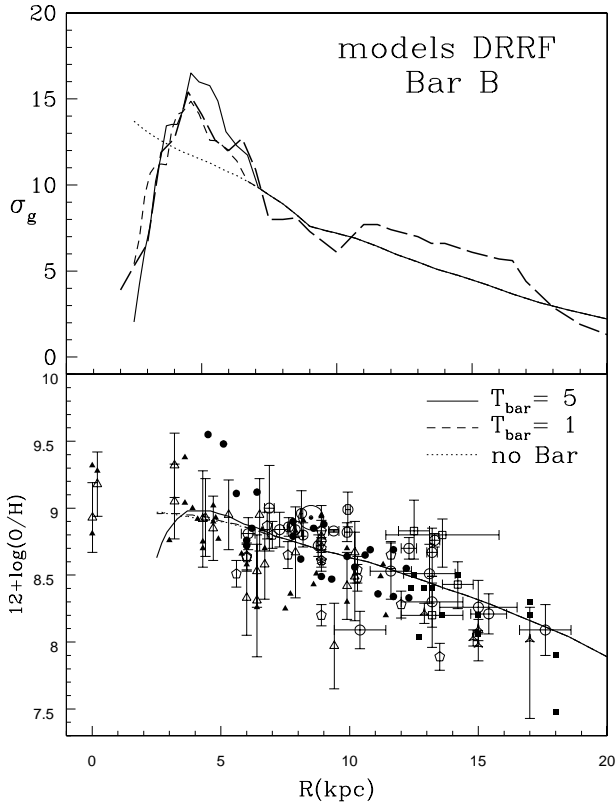


**Fig. 14.** Models DRRF mimicking case B for the Galactic Bar, adopting the flow patterns of Fig. 13. Disregard abundance data at  $r = 0$  (see text).

ful” overall inflow pattern (§5). The relevant models with their detailed velocity patterns, for the usual two values of  $T_{bar}$ , are shown in Figs. 13 and 14. Notice once again that rather low drift velocities ( $|v| < 0.5$  km sec) suffice to reproduce the gas peak, which reinforces the plausibility of the models.

In case B models, the metallicity gradient is clearly affected in the inner regions by the switch in the gas flow pattern, at least if this lasted for some time (Fig. 14, case  $T_{bar} = 5$ ). This feature, though, is again hard to check from observations since there are no tracers of Disc metallicity for  $r < 4$  kpc (see §6.1).

Case B can also reproduce the observed gas profile combined with an Oort-type SF law with  $\kappa = 1$  (model O10RF), especially provided the Bar formed recently, as displayed in Fig. 16 with  $T_{bar} = 1$ . If the Bar-induced flows activate much earlier, the predicted peak is very sharp and narrow (Fig. 16, case  $T_{bar} = 5$  Gyr), due to the milder sensitivity of SF to the gas density in this case (Schmidt-like exponent  $\kappa = 1$ ): with respect to other SF laws, this SF is relatively less efficient where the gas density is high, namely where the gas accumulates around 4.5 kpc, while it is relatively more efficient where the density drops, below 4 kpc. Such a sharp peak seems in con-

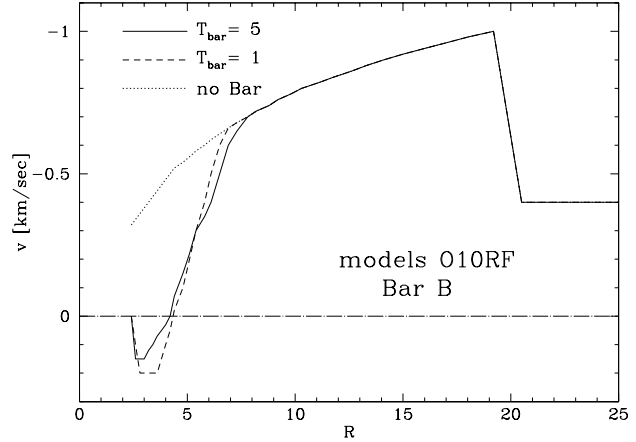


**Fig. 15.** Radial flow velocity pattern adopted from  $t_G - T_{bar}$  upon the base “no Bar” inflow pattern, to mimic case B for the Galactic Bar with models O10RF.

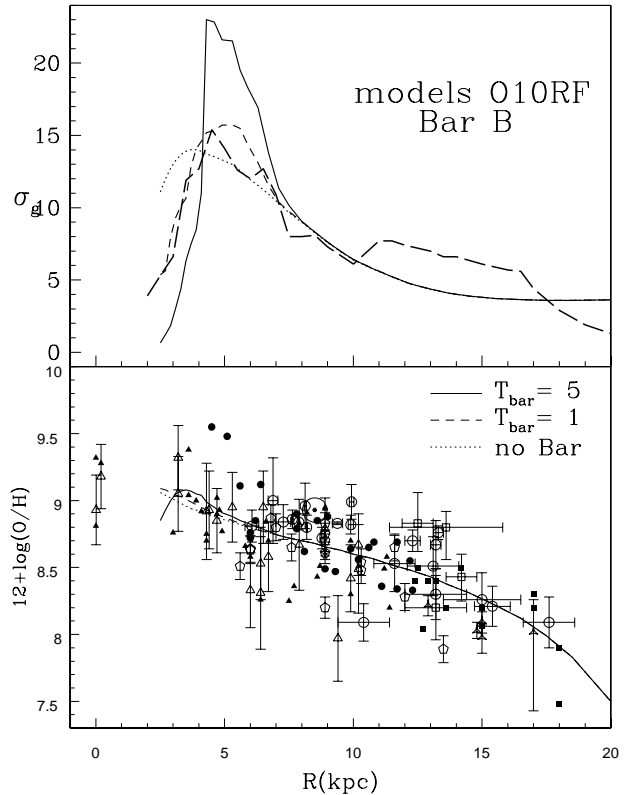


**Fig. 16.** Models O10RF mimicking case B for the Galactic Bar, adopting the flow patterns of Fig. 15.

trast with the observed, quite broad distribution (the observational uncertainty on the gas density profile in the inner Galactic region is less than a factor of 2, Dame 1993). Models O10RF with an “old” Bar are therefore less appealing in case B.

### 6.3. Concluding remarks

We referred to the current understanding of the structure and features of the Galactic Bar to simulate its dynamical influence on the surrounding gas flows and distribution. Chemical models accounting for the effect of the Bar make it finally possible to reproduce the gas profile properly, which could not be accomplished by static models (PC99).

Broadly speaking, two main scenarios are presented.

1. The Bar stretches to 3.5 kpc and the gas peak is due to a rapid depletion of gas drifting from the Bar’s CR to the Galactic Centre (case A). To reproduce the gas profile, we need a gas distribution which keeps increasing from the outer disc inward, down to  $\sim 4$  kpc where the Bar’s influence produces the sharp depletion. This can be achieved only by means of efficient radial inflows over the whole disc, and in this case radial inflows are also the major source for the observed metallicity gradients (models S15RFe and O10RFe).
2. The Bar ends around 2.5 kpc, where its CR is set, and the gas peak is due to the accumulation of gas from CR outward to its OLR at  $\sim 4.5$  kpc (case B). A rather limited contribution of radial inflows from the outer regions suffices to obtain the peak. In this case, the metallicity gradients in the outer regions of the disc may be mainly due to the SF process itself, and to the intrinsic variation of the SF efficiency with radius (model DRRFe).

Within these simplified models it is unfeasible to discuss any further on the scenarios for Bar structure and age, and related gas flows. Only detailed dynamical simulations for Bar formation, evolution and potential can tell how the molecular ring consequently formed, which is beyond the goals of this paper (see also §7). Here we were just interested in showing how even simple qualitative models for Bar-induced gas flows in the inner disc solve in fact the puzzle encountered in PC99. Namely, they can reproduce at the same time both the metallicity gradient and the gas distribution, in particular the peak corresponding to the molecular ring around 4 kpc. This can be accomplished already with quite slow, and largely plausible, flow velocities. The present modelling therefore provides a simple tool for qualitative understanding of possible behaviours.

Regardless of details, however, one condition is necessary for the scheme to work: there must be enough gas in the inner regions of the Disc, which the Bar can then “shape” to resemble the detailed observed distribution. This favours chemical models with radial inflows where the metallicity gradient can coexist with high gas fractions in the inner shells. Our simulations showed that no Bar-induced gas flow superimposed on otherwise static models (as those by PC99) can produce the observed gas peak: whatever the assumed age of the Bar or gas velocity profile, there is not enough gas left in the inner Galactic regions if we are to reproduce the metallicity gradient

as well. Gas must be continuously replenished by inflows from outer regions; that’s why we presented here “barred” models based only on the “successful” models with radial inflows from §5 and never on the static models of PC99.

## 7. Summary and conclusions

From the results of static chemical models, PC99 underlined the need to introduce radial flows to explain some features of the Galactic Disc. In fact, static models are unable to reproduce, at the same time, both the metallicity gradient and the radial gas profile; in particular, the peak corresponding to the molecular ring at 4–6 kpc is likely to be a consequence of gas drifts induced by the dynamical influence of the Galactic Bar. Therefore, in the present paper we introduced a new chemical model including radial gas flows, developed as a multi-dimensional generalization of the original static model (§3). Our model is conceived so as to adapt to any imposed radial velocity profile, describing both inflows and outflows in any part of the disc. The model is carefully tested against instability problems and spatial resolution, by comparing it to suitable exact analytical cases (Appendix B). In this paper we applied the model to the Galactic Disc; more in general, such models allowing for gas drifts are meant to be used as fast and handy interfaces between detailed dynamical galaxy models (predicting the velocity profiles) and parametric chemical and spectro-photometric models.

An overview of the behaviour of chemical models with radial inflows of gas shows that these provide an alternative “dynamical” assumption to the inside-out disc formation scenario to explain the metallicity gradient (§4). With radial gas flows, the model can reproduce the metallicity gradient even in the case of a Schmidt or an Oort-type SF law, which were excluded in the case of static models (see PC99). In addition, it appears that even low radial flow velocities, well within observational limits and theoretical expectations (see §2), have non-negligible effects upon model predictions on the metallicity gradient and moreover on the gas distribution. In particular, if radial gas inflows are allowed for, a metallicity gradient can coexist with a high gas fraction in the inner regions, at odds with simple static models. This is indispensable to reproduce the observed gas distribution in the inner Galaxy (see point 2 below). The remarkable effects of even slow radial flows upon observable quantities, mainly upon the gas distribution, should be kept in mind as a caveat when comparing real galaxies to simple analytical models which predict a one-to-one relationship between metallicity and gas fraction (e.g. Tinsley 1980). Our models show that small dynamical effects, like slow gas flows, can easily make real systems depart from the behaviour of simple models.

With our model it is possible to mimic the dynamical influence of the Galactic Bar and reproduce the peak in the gas distribution around 4 kpc (§6). Two scenarios,

related to two different models for the structure of the Bar, are qualitatively suggested.

- A. With a Schmidt or an Oort-type SF law, slow radial inflows in the disc pile up gas inward down to  $r = 3.5 - 4$  kpc. Here, the Bar CR radius is found and the gas is quickly swept inward from CR toward an ILR, which causes the drop in the gas profile at 3.5 kpc.
- B. With a SF law like that by Dopita & Ryder (1994), smaller inflow rates suffice to reproduce the metallicity gradient, leading to a lower concentration of gas in the inner regions than in the previous case. The peak corresponding to the molecular ring can be reproduced with a Bar CR around 2.5 kpc and its OLR around 4.5 kpc, so that all the gas external to  $r = 2.5$  kpc tends to pile up around the OLR.

Though these models are just qualitative and cannot describe the detailed dynamical process of Bar formation nor the evolution of the related gas flows to form the molecular ring, they provide two interesting indications.

1. Only when introducing the effects of the Bar, the model is able to reproduce the radial gas profile properly. The only possible exception resides in a particular combination of an Oort-type SF law with a radial inflow pattern whose velocity decreases inward (model O10RFe; this combination may lead to a peak of the gas distribution in the inner Galactic regions, closed to the observed molecular ring. But this particular, fortunate case does not diminish the general conclusions about the role of the Galactic Bar.
2. In any case (A or B above), overall radial inflows in the disc are indispensable to replenish the inner regions with enough gas that the observed molecular ring can form under the influence of the Bar. This seems to favour disc models with radial inflows, unless one assumes that the gas in the ring has some different origin (gas swept from the Bulge, or accreted later).

To investigate these issues any further, detailed gas-dynamical models are obviously required. Unfortunately, most studies on Bar-induced gas dynamics (see references in §6) concentrate on the observed features of the very inner regions, such as the nuclear ring, the 3 kpc expanding arm, and so forth. Little discussion can be found about the effects of the Bar on more external regions, and on the formation of the molecular ring in particular: whether it is due to gas depletion inside CR as in our case A, or due to gas accumulation at some resonance (e.g. Binney et al. 1991, Fux 1999) as in our case B, or whether it just consists of two or more tightly wound spiral arms (e.g. Englmaier & Gerhard 1999). Further gas-dynamical studies suggesting detailed scenarios, time-scales, and velocity profiles for the formation of the molecular ring would be welcome, for the sake of including the effects of the Bar in chemical evolution models more consistently.

Further investigation of gas-dynamical models on the influence of the Bar on even larger scales (namely, outside its OLR) should be pursued as well, since this is a clue issue related to a claimed discrepancy between the characteristics of the Galactic Bar and the observed metallicity gradient. It is well known that barred galaxies display systematically shallower gradients than ordinary spirals (e.g. Alloin et al. 1981, Vila-Costas & Edmunds 1992, Martin & Roy 1994). This is likely a consequence of the radial mixing induced by bars; in fact, Martin & Roy (1994) found a correlation for external galaxies between the strength of a bar and the metallicity gradient. Taking this empirical relation at face value, the Galactic Bar with an axial ratio of  $\sim 0.5$  should induce a metallicity gradient of  $-0.03$  dex/kpc, much shallower than the observed one of  $-0.07$  dex/kpc, which is typical of a *normal* Sbc galaxy. To overcome such a puzzle, it has been suggested that the Galactic Bar must be very young ( $< 1$  Gyr), so that there was not enough time yet to flatten the gradient (Gummersbach et al. 1998); but this is in conflict with other estimates of the Bar's age (e.g. Sevenster 1997, 1999). Alternatively, we suggest that the discrepancy might be only apparent, since the Galactic Bar is quite small, and the Milky Way cannot be properly considered a barred spiral. It might be unlikely that the Bar can influence the metallicity gradient all over the Disc, as in really barred galaxies: Bar-induced radial drifts and corresponding chemical mixing are expected to occur from CR toward the ILR (inflows) and to the OLR (outflows; e.g. Schwarz 1981, 1984; Friedli et al. 1994). Present understanding of the Galactic Bar sets its OLR between 4.5 and 6 kpc (§6 and references therein), so in our models we presumed that the Bar induces negligible mixing beyond these radii, regardless of its age (see also Gerhard 1999). If the situation is as in the models we presented here, in fact, the metallicity gradient in the outer regions is unperturbed and just related to intrinsic Disc properties and/or large-scale viscous flows.

However, gas-dynamical simulations dedicated to the effects of the Galactic Bar over the whole Disc would be necessary, so as to investigate the relation between the Bar, radial mixing and the metallicity gradient more consistently. More in general, including the effects of bar-induced radial flows in the picture of the chemical evolution of spiral galaxies might turn out to be of wide interest, since it is likely that all spirals develop at some point, or have developed in the past, some bar-like structure (Binney 1995). Infrared observations indeed reveal that a large fraction of spirals host a barred structure (e.g. Eskridge et al. 1999), and recent numerical simulations suggest that even weak bars or oval distortions may be able to induce radial drifts to form multiple gaseous rings at the corresponding Lindblad resonances (Jungwiert & Palouš 1996). Bars could even drive secular evolution of spiral discs from late to early type (e.g. Dutil & Roy 1999). Bar-driven radial gas flows might therefore play a fundamental role in the chemical evolution of spiral discs.



*Acknowledgements.* We thank Joachim Köppen for his advice on numerical modelling of radial gas flows, Yuen K. Ng and Antonella Vallenari for useful discussions about Galactic structure, and our referee, Mike Edmunds, whose suggestions much improved the presentation of our paper.

L.P. acknowledges kind hospitality from the Nordita Institute in Copenhagen, from the Observatory of Helsinki and from Sissa/Isas in Trieste. This study has been financed by the Italian MURST through a PhD grant and the contract “Formazione ed evoluzione delle galassie”, n. 9802192401.

## Appendix A: The explicit expression of Eq. (18)

Here we sort out the explicit expression (20) of the solution (18) for  $G_i(r_k, t)$ , by calculating the matrix  $e^{t\mathcal{A}}$ . Let us first introduce the simplified notation:

$$G_k(t) = G_i(r_k, t), \quad \overline{W}_k = \overline{W}_i(r_k) \quad (\text{A1})$$

For the sake of example, we present here the detailed solution in the case of three shells ( $N = 3$ ). The relevant system of equations (17) becomes:

$$\begin{cases} \frac{d}{dt} G_1(t) = \vartheta_1 G_1(t) + \gamma_1 G_2(t) + W_1 \\ \frac{d}{dt} G_2(t) = \alpha_2 G_1(t) + \vartheta_2 G_2(t) + \gamma_2 G_3(t) + W_2 \\ \frac{d}{dt} G_3(t) = \alpha_3 G_2(t) + \vartheta_3 G_3(t) + W_3 + \overline{\omega}_i \end{cases} \quad (\text{A2})$$

where all the coefficients are considered as constants (see §3.2), though we have omitted the bar over  $W_k$  and  $\vartheta_k$  for simplicity. A system like (A2) holds for each chemical species  $i$ , but the characteristic matrix  $\mathcal{A}$  is the same for any  $i$  (see §3.2); in this case:

$$\mathcal{A} = \begin{pmatrix} \vartheta_1 & \gamma_1 & 0 \\ \alpha_2 & \vartheta_2 & \gamma_2 \\ 0 & \alpha_3 & \vartheta_3 \end{pmatrix}$$

Let's first notice, from the definition (9), that  $\gamma_k$  and  $\alpha_{k+1}$  can never be both positive: at least one of them must be zero since they are “activated” in the opposite cases of inflow or outflow at  $r_{k+\frac{1}{2}}$ , respectively; if there is no flow at all through  $r_{k+\frac{1}{2}}$ , they both reduce to zero. Therefore, in our calculations we are always entitled to use the condition:

$$\gamma_k \alpha_{k+1} = 0 \quad \forall k \quad (\text{A3})$$

The eigenvalues of the matrix  $\mathcal{A}$  are

$$\lambda_{1,2,3} = \vartheta_{1,2,3}$$

and the associated eigenvectors are:

$$\mathbf{u}_1 = \begin{pmatrix} 1 \\ \frac{\alpha_2}{\vartheta_1 - \vartheta_2} \\ \frac{\alpha_3}{\vartheta_1 - \vartheta_3} \end{pmatrix} \mathbf{u}_2 = \begin{pmatrix} \frac{\gamma_1}{\vartheta_2 - \vartheta_1} \\ 1 \\ \frac{\alpha_3}{\vartheta_2 - \vartheta_3} \end{pmatrix} \mathbf{u}_3 = \begin{pmatrix} \frac{\gamma_1}{\vartheta_3 - \vartheta_1} \frac{\gamma_2}{\vartheta_3 - \vartheta_2} \\ \frac{\gamma_2}{\vartheta_3 - \vartheta_2} \\ 1 \end{pmatrix}$$

From (19) we get:

$$e^{t\mathcal{A}} = \begin{pmatrix} e^{\vartheta_1 t} & \gamma_1 f_{21}(t) & \frac{\gamma_1 \gamma_2}{\vartheta_3 - \vartheta_2} [f_{31}(t) - f_{21}(t)] \\ \alpha_2 f_{21}(t) & e^{\vartheta_2 t} & \gamma_2 f_{32}(t) \\ \frac{\alpha_2 \alpha_3}{\vartheta_2 - \vartheta_1} [f_{32}(t) - f_{31}(t)] & \alpha_3 f_{32}(t) & e^{\vartheta_3 t} \end{pmatrix}$$

where we have indicated with:

$$f_{kl}(t) = f_{lk}(t) \equiv \frac{e^{\vartheta_k t} - e^{\vartheta_l t}}{\vartheta_k - \vartheta_l}, \quad k, l = 1, 2, 3$$

Defining:

$$g_k(\Delta t) \equiv \int_{t_0}^{t_1} e^{\vartheta_k(t_1-t)} dt = \frac{e^{\vartheta_k \Delta t} - 1}{\vartheta_k}$$

the solution (18) in the case  $N = 3$  becomes:

$$\begin{cases} G_1(t_1) = e^{\vartheta_1 \Delta t} G_1(t_0) + \\ \quad + \gamma_1 \frac{e^{\vartheta_2 \Delta t} - e^{\vartheta_1 \Delta t}}{\vartheta_2 - \vartheta_1} G_2(t_0) + \\ \quad + \gamma_1 \gamma_2 \frac{f_{31}(\Delta t) - f_{21}(\Delta t)}{\vartheta_3 - \vartheta_2} G_3(t_0) + \\ \quad + W_1 \frac{e^{\vartheta_1 \Delta t} - 1}{\vartheta_1} + \\ \quad + \gamma_1 \frac{W_2}{\vartheta_2 - \vartheta_1} \left( \frac{e^{\vartheta_2 \Delta t} - 1}{\vartheta_2} - \frac{e^{\vartheta_1 \Delta t} - 1}{\vartheta_1} \right) + \\ \quad + \gamma_1 \gamma_2 \frac{W_3}{\vartheta_3 - \vartheta_2} \left[ \frac{g_3(\Delta t) - g_1(\Delta t)}{\vartheta_3 - \vartheta_1} - \frac{g_2(\Delta t) - g_1(\Delta t)}{\vartheta_2 - \vartheta_1} \right] \\ G_2(t_1) = \alpha_2 \frac{e^{\vartheta_2 \Delta t} - e^{\vartheta_1 \Delta t}}{\vartheta_2 - \vartheta_1} G_1(t_0) + \\ \quad + e^{\vartheta_2 \Delta t} G_2(t_0) + \\ \quad + \gamma_2 \frac{e^{\vartheta_3 \Delta t} - e^{\vartheta_2 \Delta t}}{\vartheta_3 - \vartheta_2} G_3(t_0) + \\ \quad + \alpha_2 \frac{W_1}{\vartheta_2 - \vartheta_1} \left( \frac{e^{\vartheta_2 \Delta t} - 1}{\vartheta_2} - \frac{e^{\vartheta_1 \Delta t} - 1}{\vartheta_1} \right) + \\ \quad + W_2 \frac{e^{\vartheta_2 \Delta t} - 1}{\vartheta_2} + \\ \quad + \gamma_2 \frac{W_3}{\vartheta_3 - \vartheta_2} \left( \frac{e^{\vartheta_3 \Delta t} - 1}{\vartheta_3} - \frac{e^{\vartheta_2 \Delta t} - 1}{\vartheta_2} \right) \\ G_3(t_1) = \alpha_2 \alpha_3 \frac{f_{32}(\Delta t) - f_{31}(\Delta t)}{(\vartheta_2 - \vartheta_1)} G_1(t_0) + \\ \quad + \alpha_3 \frac{e^{\vartheta_3 \Delta t} - e^{\vartheta_2 \Delta t}}{\vartheta_3 - \vartheta_2} G_2(t_0) + \\ \quad + e^{\vartheta_3 \Delta t} G_3(t_0) + \\ \quad + \alpha_2 \alpha_3 \frac{W_1}{\vartheta_2 - \vartheta_1} \left[ \frac{g_3(\Delta t) - g_2(\Delta t)}{\vartheta_3 - \vartheta_2} - \frac{g_3(\Delta t) - g_1(\Delta t)}{\vartheta_3 - \vartheta_1} \right] + \\ \quad + \alpha_3 \frac{W_2}{\vartheta_3 - \vartheta_2} \left( \frac{e^{\vartheta_3 \Delta t} - 1}{\vartheta_3} - \frac{e^{\vartheta_2 \Delta t} - 1}{\vartheta_2} \right) + \\ \quad + (W_3 + \overline{\omega}_i) \frac{e^{\vartheta_3 \Delta t} - 1}{\vartheta_3} \end{cases} \quad (\text{A4})$$

With zero flow velocity ( $\alpha_k = \beta_k = \gamma_k = 0$ ), (A4) reduces to the solving formula of the original static model (see PCB98). Notice that the solution  $G_1(t_1)$  for the 1<sup>st</sup> shell includes not only the contribution of the contiguous 2<sup>nd</sup> shell, but also a contribution from the 3<sup>rd</sup> shell “scaled” by its passage through the 2<sup>nd</sup> shell. Similarly, the 3<sup>rd</sup> shell is affected not only by the 2<sup>nd</sup>, but also by the 1<sup>st</sup> shell though they are not contiguous.

With analogous procedure, for an arbitrary number  $N$  of shells the solution is of the kind:

$$G_k(t) = \sum_{l=1}^N F_{kl}(\Delta t) G_l(t_0) + \sum_{m=0}^N H_{km}(\Delta t) W_m \quad (\text{A5})$$

where:

$$\begin{aligned} F_{kk}(\Delta t) &= e^{\vartheta_k \Delta t} \\ F_{kl}(\Delta t) &= \gamma_k \gamma_{k+1} \dots \gamma_{l-1} \mathcal{F}_{k(k+1) \dots l}(\Delta t) & l > k \\ F_{kl}(\Delta t) &= \alpha_{l+1} \dots \alpha_{k-1} \alpha_k \mathcal{F}_{l(l+1) \dots k}(\Delta t) & l < k \\ H_{kk}(\Delta t) &= g_k(\Delta t) \\ H_{kl}(\Delta t) &= \gamma_k \gamma_{k+1} \dots \gamma_{l-1} \mathcal{H}_{k(k+1) \dots l}(\Delta t) & l > k \\ H_{kl}(\Delta t) &= \alpha_{l+1} \dots \alpha_{k-1} \alpha_k \mathcal{H}_{k(k-1) \dots l}(\Delta t) & l < k \end{aligned}$$

and the quantities  $\mathcal{F}$  and  $\mathcal{H}$  are constructed by means of recursive formulæ:

$$\begin{aligned}
 \mathcal{F}_{ki}(\Delta t) &= f_{ki}(\Delta t) & \mathcal{H}_{ki}(\Delta t) &= \frac{g_k \Delta t - g_i \Delta t}{\vartheta_k - \vartheta_i} \\
 \mathcal{F}_{kij} &= \frac{\mathcal{F}_{ki} - \mathcal{F}_{kj}}{\vartheta_i - \vartheta_j} & \mathcal{H}_{kij} &= \frac{\mathcal{H}_{ki} - \mathcal{H}_{kj}}{\vartheta_i - \vartheta_j} \\
 \mathcal{F}_{kijm} &= \frac{\mathcal{F}_{kij} - \mathcal{F}_{kim}}{\vartheta_j - \vartheta_m} & \mathcal{H}_{kijm} &= \frac{\mathcal{H}_{kij} - \mathcal{H}_{kim}}{\vartheta_j - \vartheta_m} \\
 \mathcal{F}_{kijmn} &= \frac{\mathcal{F}_{kijm} - \mathcal{F}_{kijn}}{\vartheta_m - \vartheta_n} & \mathcal{H}_{kijmn} &= \frac{\mathcal{H}_{kijm} - \mathcal{H}_{kijn}}{\vartheta_m - \vartheta_n} \\
 \vdots & & \vdots &
 \end{aligned}$$

The coefficients  $F_{kl}$  and  $H_{kl}$  describe the contribution of the generic shell  $l$  to the chemical evolution of  $k$ . Notice that a shell external to  $k$  ( $l > k$ ) can influence  $k$  only if all the inflow coefficients  $\gamma$  in between  $l$  and  $k$  are non-zero, namely if there is a continuous inflow from  $l$  to  $k$ , as expected. The same holds for inner shells  $l < k$ , whose contribution  $F_{kl}$ ,  $H_{kl}$  is non-zero only if none of the intermediate outflow coefficients  $\alpha$  is zero. The solution (A5) gets more and more complicated the larger the number  $N$  of shells considered, since each shell formally feels the contribution of all the other shells (as already noticed in the above case  $N = 3$ ). This occurs because (A5) would be the exact analytical solution in the case of a differential system with constant coefficients, namely if the  $\mathcal{A}$  matrix in (17) were constant. Then, (A5) would describe the complete evolution of any shell  $k$ , which over a galaxy’s lifetime would indeed process and exchange gas drifting from or to rather distant shells. But  $\mathcal{A}(t)$  is not constant even when the flow pattern  $\alpha$ ,  $\beta$ ,  $\gamma$  is constant, because  $\eta_k(t)$  and therefore  $\vartheta_k(t)$  evolve in time due to SF; in fact, we apply (A5) only upon short timesteps  $\Delta t$ , within which  $\mathcal{A}(t)$  can be considered approximately constant. If  $\Delta t$  is short enough with respect to the radial flow velocities — as guaranteed by the Courant condition  $\Delta t < v\Delta r$ , see §3.2 —, we can assume that within  $\Delta t$  the  $k$ -th shell is affected just by the flows from the contiguous shells  $k+1$  and  $k-1$ , and not from more distant shells, although all of them formally contribute to the solution. In this approximation we neglect all higher order terms in  $\alpha$  and  $\gamma$ , namely all the terms  $\mathcal{O}(\alpha_i\alpha_j)$  and  $\mathcal{O}(\gamma_i\gamma_j)$ , keeping only the “linear” terms of the kind  $\alpha_k f_{k(k-1)}$  and  $\gamma_k f_{k(k+1)}$ ; so the general solution (A5) reduces in fact to (20).

### Appendix B: Testing the numerical model

Since discretized numerical solutions for partial differential equations containing an “advection term” tend to be affected by instability problems (e.g. Press et al. 1986), we tested our numerical code with gas flows against suitable analytical cases. We report here two representative tests involving pure gas flows (no SF) which allow for exact analytical solutions; to these we compare the predictions of our numerical code with a SF efficiency dropped virtually to zero.

*Selecting the timestep.* The first reference analytical case is that of a purely gaseous disc of infinite radial extent and flat profile, where the gas is:

1. accreting uniformly with a time-scale  $\tau$ ;

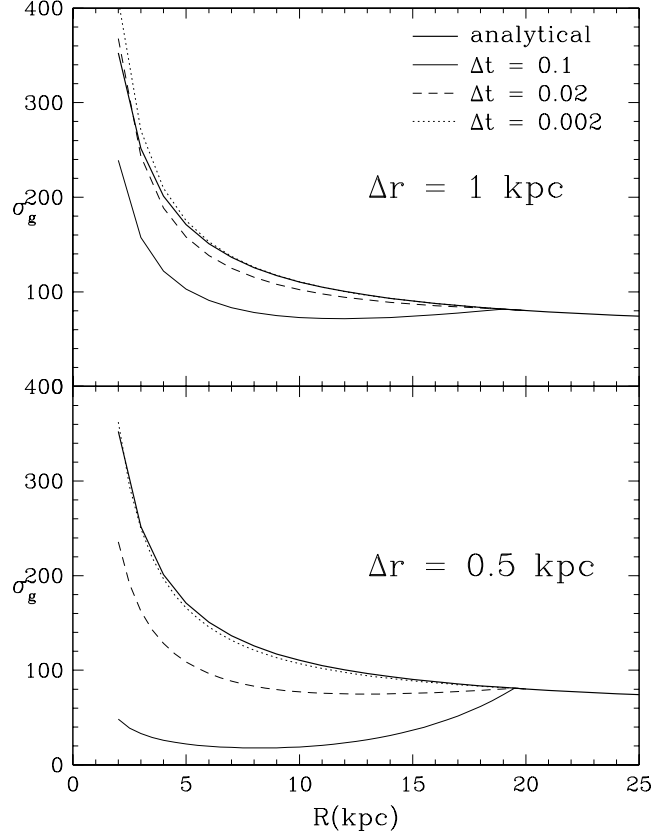


**Fig. B1.** Numerical models compared to the exact analytical solution for a flat accretion profile with inflows. Different models correspond to different typical timesteps (see legend on top right) and to different shell spacing (upper to lower panel).

2. flowing inward with a constant (in time) and uniform (in space) velocity  $v$ , starting from the “inflow onset time”  $T_{rf}$ .

Such a system is governed by the same differential equation (13) describing the adopted boundary condition at the outer disc edge in the chemical model (§3.1.2). Eq. (13) is a linear, first order, partial differential equation, equivalent to the system:

$$\begin{cases} \frac{dr}{dt} = v & (a) \\ \frac{d\sigma}{dt} = A e^{-\frac{t}{\tau}} - \frac{v}{r} \sigma & (b) \end{cases} \quad (B1)$$

Eq. (B1a) is solved as:

$$r = v(t - t_0) + r_0$$

and substitution into Eq. (B1b) yields:

$$\frac{d\sigma}{dt} + \frac{1}{t+p} \sigma = A e^{-\frac{t}{\tau}} \quad p \equiv \frac{r_0}{v} - t_0 \quad (B2)$$

This linear, first order, ordinary differential equation is solved as:

$$\begin{aligned} \sigma(t) &= \sigma(t_0) e^{-\int_{t_0}^t \frac{1}{\xi+p} d\xi} + \int_{t_0}^t e^{-\int_{\xi}^t \frac{1}{\theta+p} d\theta} A e^{-\frac{\xi}{\tau}} d\xi \\ &= \sigma(t_0) \frac{t_0+p}{t+p} + \frac{A}{t+p} \tau \times \\ &\quad \times \left[ (t_0+p) e^{-\frac{t_0}{\tau}} - (t+p) e^{-\frac{t}{\tau}} + \tau \left( e^{-\frac{t_0}{\tau}} - e^{-\frac{t}{\tau}} \right) \right] \end{aligned}$$

Finally, replacing back:

$$r_0 = r - v(t - t_0), \quad t + p = \frac{r}{v}$$

we get:

$$\begin{aligned} \sigma(r, t) &= \left[ 1 - \frac{v}{r}(t - t_0) \right] \sigma(r - v(t - t_0), t_0) + A \tau \times \\ &\quad \times \left[ \left( 1 - \frac{v}{r}(t - t_0) \right) e^{-\frac{t_0}{\tau}} - e^{-\frac{t}{\tau}} + \frac{v}{r} \tau \left( e^{-\frac{t_0}{\tau}} - e^{-\frac{t}{\tau}} \right) \right] \end{aligned} \quad (\text{B3})$$

Let's now set the initial conditions at  $t_0$ . If radial flows “activate” at a time  $t_0 = T_{rf} \geq 0$  the surface density distribution for  $t \leq T_{rf}$  is determined just by the accretion profile:

$$\sigma(r, T_{rf}) = A \tau \left( 1 - e^{-\frac{T_{rf}}{\tau}} \right)$$

(see Eq. 2) and Eq. (B3) becomes in fact Eq. (14). Here in our test case, Eq. (14) is the exact analytical description of the surface density profile over the whole disc (a part from the centre  $r = 0$ , which is a singular point).

As a representative test, let's consider the case  $\tau = 3$  Gyr,  $T_{rf} = 0$  and  $v = -1$  km sec<sup>-1</sup>. The relevant analytical solution is plot in Fig. B1 for  $t = t_G = 15$  Gyr (thick solid line). The numerical models used for comparison cover the radial range 2 to 20 kpc and adopt a flat accretion profile  $A(r) \equiv A$ . Their outer edge does match exactly with the analytical counterpart, since the boundary condition at  $r = 20$  kpc is given by the analytical expression (14) itself. But the predictions of numerical models at inner radii tend to deviate from the reference density profile, and the mismatch is larger:

1. the larger the typical timestep of the model;
2. for a fixed timestep, the thinner the shells (compare upper to lower panel).

For a typical shell width of 1 kpc, for instance, a good match is obtained with model timesteps of  $2 \times 10^{-2}$  Gyr, while model shells of 0.5 kpc an acceptable profile is obtained only with timesteps of  $2 \times 10^{-3}$  Gyr. Therefore, a reliable representation of radial gas flows is obtained only with a suitably small timestep; how small, is related to the width of the shells, namely to the resolution of the grid spacing.

*Selecting the grid spacing.* Since our models are to simulate a disc with an exponential profile, as a second test we consider a gaseous disc with uniform and constant inflow time-scale and inflow velocity, analogous to the previous case, but with an exponential profile. Namely, in the representative differential equation (12) the accretion profile  $A(r)$  declines exponentially outward:

$$A(r) = A(r_\odot) e^{-\frac{r-r_\odot}{r_d}}$$

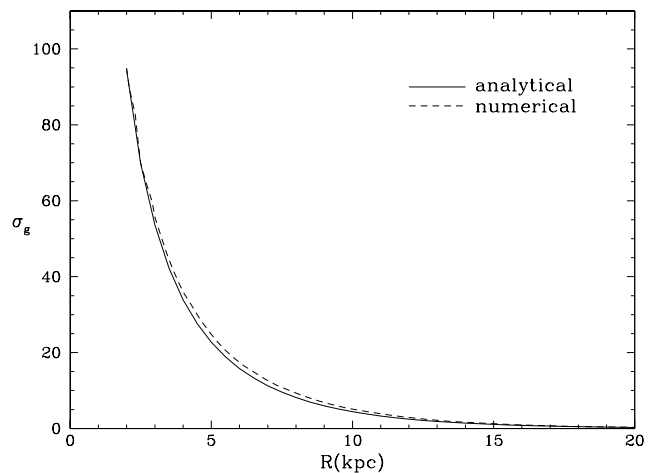


**Fig. B2.** Exact analytical solution for an exponential accretion profile with inflows compared to a numerical model with 40 shells equally spaced in logarithmic scale.

Eq. (12) can then be written:

$$\frac{\partial \sigma}{\partial t} + v \frac{\partial \sigma}{\partial r} = A(r_\odot) e^{-\frac{r-r_\odot}{r_d}} e^{-\frac{r}{r_d}} e^{-\frac{t}{\tau}} - \frac{v}{r} \sigma$$

This is another linear, first order, partial differential equation of the same kind as (13), and can be solved with analogous procedure into:

$$\begin{aligned} \sigma(r, t) &= \left[ 1 - \frac{v}{r}(t - t_0) \right] \sigma(r - v(t - t_0), t_0) + \\ &\quad + \frac{A(r_\odot) e^{-\frac{r-r_\odot}{r_d}}}{\frac{1}{\tau} + \frac{v}{r_d}} \left[ \left( 1 - \frac{v}{r}(t - t_0) \right) e^{-\frac{t_0}{\tau} + \frac{v}{r_d}(t-t_0)} + \right. \\ &\quad \left. - e^{-\frac{t}{\tau}} + \frac{v}{r} e^{-\frac{t_0}{\tau} + \frac{v}{r_d}(t-t_0)} e^{-\frac{t}{\tau}} \right] \end{aligned} \quad (\text{B4})$$

Notice that Eq. (B3) for a flat profile is recovered from (B4) for  $r_d \rightarrow \infty$ . If radial inflows set in at time  $t_0 = T_{rf} \geq 0$ , from

$$\sigma(r, T_{rf}) = A(r_\odot) e^{-\frac{r-r_\odot}{r_d}} \tau \left( 1 - e^{-\frac{T_{rf}}{\tau}} \right)$$

we get:

$$\begin{aligned} \sigma(r, t) &= A(r_\odot) e^{-\frac{r-r_\odot}{r_d}} \left\{ \tau \left( 1 - e^{-\frac{T_{rf}}{\tau}} \right) e^{\frac{v}{r_d}(t-T_{rf})} + \right. \\ &\quad + \frac{e^{\frac{v}{r_d}t - \left(\frac{1}{\tau} + \frac{v}{r_d}\right)T_{rf}} - e^{-\frac{t}{\tau}}}{\frac{1}{\tau} + \frac{v}{r_d}} + \\ &\quad + \frac{v}{r} \left[ \frac{e^{\frac{v}{r_d}t - \left(\frac{1}{\tau} + \frac{v}{r_d}\right)T_{rf}} - e^{-\frac{t}{\tau}}}{\left(\frac{1}{\tau} + \frac{v}{r_d}\right)^2} - (t - T_{rf}) \times \right. \\ &\quad \left. \left. \times \left( \tau \left( 1 - e^{-\frac{T_{rf}}{\tau}} \right) e^{\frac{v}{r_d}(t-T_{rf})} + \frac{e^{\frac{v}{r_d}t - \left(\frac{1}{\tau} + \frac{v}{r_d}\right)T_{rf}}}{\frac{1}{\tau} + \frac{v}{r_d}} \right) \right] \right\} \end{aligned} \quad (\text{B5})$$

We compared this second analytical case to our numerical model, where an exponential accretion profile was adopted between 2 and 20 kpc, and at the outer edge the boundary condition (14) was replaced by (B5). Our tests showed that in this case the analytical profile is better reproduced the larger the number of shells, i.e. the finer the grid spacing. A good match is

obtained especially when model shells are equally spaced in the logarithmic, rather than linear, scale; namely when the shells are chosen, in this case of an exponential accretion profile, so as to contain roughly the same mass, rather than cover the same radial width. Fig. B2 shows in fact the analytical solution (B5) (for  $r_d = 4$  kpc,  $\tau = 3$ ,  $T_{rf} = 0$  and  $v = -1$ ) together with a corresponding numerical model with 40 shells logarithmically spaced (from 0.1 kpc wide for the inner ones to  $\sim 1$  kpc wide for the outer ones).

With such a grid spacing, our tests with the reference flat profile of Fig. B1 indicate  $10^{-4}$  Gyr as a suitable timestep to obtain stable solutions for velocities up to the order of  $1 \text{ km sec}^{-1}$ .

In the light of all these tests, in our chemical models we adopted a grid spacing of 35 shells from 2.5 to 20 kpc, equally spaced in logarithmic scale and a typical timestep of  $10^{-4}$  Gyr (see §3.2). Of course, the suitable timestep depends also on the velocity field: flows with higher velocities require shorter integration timesteps. Whenever we need to consider much larger speeds than  $1 \text{ km sec}^{-1}$ , as might be the case for the strong flows induced by the Bar, we reduce the timestep in proportion.

## References

- Alloin D., Edmunds M.G., Lindblad P.O., Pagel B.E.J., *A&A* 101, 377
- Bertin G., Lin C.C., 1996, *Spiral structure in galaxies – A density wave theory*, MIT Press, Cambridge, Massachusetts
- Binney J.J., 1995, *S&T* 89, 20
- Binney J.J., Gerhard O.E., Stark A.A., Bally J., Uchida K.I., 1991, *MNRAS* 252, 210
- Binney J.J., Gerhard O.E., Spergel D.N., 1997, *MNRAS* 288, 365
- Blitz L., Spergel D.N., 1991, *ApJ* 379, 631
- Chamcham K., Tayler R.J., 1996, *MNRAS* 266, 282
- Clarke C.J., 1989, *MNRAS* 238, 283
- Combes F., Gerin M., 1985, *A&A* 150, 327
- Dame T.M., 1993, in *Back to the Galaxy* S. Holt, F. Verter (eds.), p. 267
- Dopita M.A., Ryder S.D., 1994, *ApJ* 430, 163
- Dutil Y., Roy J.R., 1999, *ApJ* 516, 62
- Dwek E., Arendt R.G., Hauser M.G., et al., 1995, *ApJ* 445, 716
- Edmunds M.G., Greenhow R.M., 1995, *MNRAS* 272, 241
- Englmeier P., Gerhard O.E., 1999, *MNRAS* 304, 512
- Eskridge P.B., Frogel J.A., Pogge R.W., Quillen A.C., Davies R.L., et al., 1999, *ApJ* in press (astro-ph 9910479)
- Fich M., Silkey M., 1991, *ApJ* 366, 107
- Friedli D., Benz W., Kennicutt R.C., 1994, *ApJ* 430, L10
- Fux R., 1997, *A&A* 327, 983
- Fux R., 1999, *A&A* 345, 787
- Gerhard O.E., 1996, *IAU Symp.* 169, 79
- Gerhard O.E., 1999, *ASP Conf. Ser.* 182 (astro-ph 9902247)
- Götz M., Köppen J., 1992, *A&A* 262, 455
- Gummersbach C.A., Kaufer A., Schäfer A.D., Szeifert T., Wolf B., 1998, *A&A* 338, 881
- Jungwiert B., Palouš J., 1996, *A&A* 311, 397
- Kennicutt R.C., 1989, *ApJ* 344, 685
- Kennicutt R.C., 1998, *ApJ* 498, 541
- Köppen J., 1994, *A&A* 281, 26
- Lacey C.G., Fall M., 1985, *ApJ* 290, 154
- Lin & Pringle, 1987, *ApJ* 320, L87
- Liszt H.S., Burton W.B., 1980, *ApJ* 236, 779
- Martin P., Roy J.R., 1994, *ApJ* 424, 599
- Martinet L., Friedli D., 1997, *A&A* 323, 363
- Mayor M., Vigroux L., 1981, *A&A* 98, 1
- Mulder W.A., Liem B.T., 1986, *A&A* 157, 148
- Ng Y.K., Bertelli G., Chiosi C., Bressan A., 1996, *A&A* 310, 771
- Nikolaev S., Weinberg M.D., 1997, *ApJ* 487, 885
- Paczynski B., Stanek K.Z., Udalski A., et al., 1994, *ApJ* 435, L113
- Peters W.L., 1975, *ApJ* 195, 617
- Pitts E., Tayler R.J., 1996, *MNRAS* 280, 1101
- Pitts E., Tayler R.J., 1989, *MNRAS* 240, 373
- Portinari L., 1998, PhD Thesis, University of Padova, Italy
- Portinari L., Chiosi C., 1999, *A&A* 350, 827 (PC99)
- Portinari L., Chiosi C., Bressan A., 1998, *A&A* 334, 505 (PCB98)
- Press W.H., Teukolsky S.A., Vetterling W.T., Flannery B.P., 1986, *Numerical recipes*, Cambridge University Press
- Quirk W.J., 1972, *ApJ* 176, L9
- Raboud D., Grenon M., Martinet L., Fux R., Udry S., 1998, *A&A* 335, L61
- Rubin R.H., Simpson J.P., Haas M.R., Erickson E.F., 1991, *ApJ* 374, 564
- Rudolph A.L., Simpson J.P., Haas M.R., Erickson E.F., Fich M., 1997, *ApJ* 489, 94
- Schwarz M.P., 1981, *ApJ* 247, 77
- Schwarz M.P., 1984, *MNRAS* 209, 93
- Sevenster M., 1997, PhD thesis, Leiden University (the Netherlands)
- Sevenster M., 1999, *MNRAS* 310, 629
- Sevenster M., Saha P., Valls-Gabaud D., Fux R., 1999, *MNRAS* 307, 584
- Shaver P.A., McGee R.X., Newton M.P., Danks A.C., Potasz S.R., 1983, *MNRAS* 204, 53
- Simpson J.P., Colgan S.W.J., Rubin R.H., Erickson E.F., Haas M.R., 1995, *ApJ* 444, 721
- Smartt S.J., Rolleston W.R.J., 1997, *ApJ* 481, L47
- Sommer-Larsen J., Yoshii Y., 1990, *MNRAS* 243, 468
- Stanek K.Z., Mateo M., Udalski A., et al., 1994, *ApJ* 429, L73
- Stanek K.Z., Udalski A., Szymanski M., et al., 1997, *ApJ* 477, 163
- Talbot R.J., Arnett D.W., 1971, *ApJ* 170, 409
- Thon R., Meusinger H., 1998, *A&A* 338, 413
- Tinsley B.M., 1980, *Fund. Cosmic Phys.* 5, 287
- Tinsley B.M., Larson R.B., 1978, *ApJ* 221, 554
- Toomre A., 1964, *ApJ* 139, 1217
- Tosi M., 1988, *A&A* 197, 33
- Unavane M., Gilmore G., 1998, *MNRAS* 295, 145
- Vila-Costas M.B., Edmunds M.G., 1992, *MNRAS* 259, 121
- Vilchez J.M., Esteban C., 1996, *MNRAS* 280, 720
- de Vaucouleurs G., 1964, *IAUS* 20, 195
- Wada K., Taniguchi Y., Habe A., Hasegawa T., 1994, *ApJ* 437, L123
- Weinberg M.D., 1992, *ApJ* 384, 81
- Weinberg M.D., 1994, *ApJ* 420, 597
- Weiner B., Sellwood J.A., 1996, *IAU Symp.* 169, 145
- Weiner B., Sellwood J.A., 1999, *ApJ* 524, 112
- Yuan C., 1993, *PASP* 105, 657
- Yoshii Y., Sommer-Larsen J., 1989, *MNRAS* 236, 779
- Zhao H.S., de Zeeuw P.T., 1998, *MNRAS* 297, 449
- Zhao H.S., Spergel D.N., Rich R.M., 1994, *AJ* 108, 2154
- Zhao H.S., Spergel D.N., Rich R.M., 1995, *ApJ* 440, L13
- Zhao H.S., Rich R.M., Spergel D.N., 1996, *MNRAS* 282, 175